IEEE Access
Multidisciplinary | Rapid Review | Open Access Journal

Received 18 September 2023, accepted 10 October 2023, date of publication 17 October 2023, date of current version 25 October 2023.

Digital Object Identifier 10.1109/ACCESS.2023.3325339

RESEARCH ARTICLE

Adaptive Robust Stability Control of All-Electrical Tank Gun Compensated by Radial Basis Neural Network

YIMIN WANG, SHUSEN YUAN, QUANZHAO SUN, XIUYE WANG, AND GUOLAI YANG
School of Mechanical Engineering, Nanjing University of Science and Technology, Nanjing 210094, China

Corresponding author: Shusen Yuan (njustyuan@163.com)

This work was supported in part by the Fundamental Research Funds for the Central Universities under Grant NS2022020, in part by the China Postdoctoral Science Foundation under Grant 2020M671494, in part by the Jiangsu Planned Projects for Postdoctoral Research Funds under Grant 2020Z179, and in part by the National Natural Science Foundation of China under Grant 52175099.

ABSTRACT Stability control of the tank gun has emerged as a pivotal issue for moving tank gun control systems (TGCS). As a complex electromechanical integrated system, TGCS of moving tank inevitably possesses significant parametric uncertainties and uncertain nonlinearities. To effectively enhance the stabilization control performance of TGCS, in this study, we introduce an adaptive robust control (ARC) strategy based on radial basis function neural network (RBFNN) compensation. The adaptive technique is employed to address the parametric uncertainties, while the RBFNN is constructed to approximate the uncertain nonlinearities and realize feedforward compensation. Subsequently, to suppress the residual uncertainties, a nonlinear robust feedback control rate is devised to strengthen the robustness of the developed controller. Lyapunov analysis shows that the proposed controller achieves uniform ultimate bounded stability. Extensive simulation and electromechanical experimental results confirm the effectiveness of the proposed controller, which shows outstanding performance in handling strong parametric uncertainties and uncertain nonlinearities.

INDEX TERMS Adaptive control, robust control, radial basis neural network, tank gun control system.

I. INTRODUCTION

The new generation of tanks is moving toward all-electric tanks, which are characterized by fewer components, a leaner structure, lower noise, and higher efficiency than the previous electro-hydraulic tanks [1]. However, the all-electric TGCS inevitably suffers from coupling, nonlinearity and uncertainty. These characteristics seriously affect the firing accuracy of the tank gun. Therefore, the problem of high-precision motion control of all-electric tanks has become a focus of development in countries around the world [2], [3]. TGCS is a complex coupled system combining mechanical system and control system [4], which directly affects the firing accuracy of tank guns. The two main problems currently faced are listed below.

First, it is very challenging to accurately model the mechanical dynamics of TGCS. TGCS is a typical mechatronics control system. The model-based highly performance controller is designed on the basis of precise dynamic modeling. In general, the more accurate the system modeling information, the better the control performance of the controller. However, constructing an accurate TGCS model has proved particularly difficult due to the tank itself having strong parametric uncertainties and complex uncertain nonlinearity [5]. Chen established an electro-mechanical-hydraulic dynamics model for a tank gun control system and designed an adaptive robust controller to effectively improve the firing accuracy of the electro-hydraulic tank [6]. However, the study did not consider the inherent uncertainty nonlinearity in the moving tank, which led to poor dynamic and steady-state performance of the control results. Sun developed a mathematical dynamics model considering the nonlinearity and uncertainty of the moving tank system

The associate editor coordinating the review of this manuscript and approving it for publication was Min Wang.

and proposed a robust control scheme to solve the problem of accurate pointing of the moving tank [7]. On the basis of this, Sun considered matched and mismatched uncertainty combined robust control techniques in following study [8], so that the uncertainties in TGCS can be further compensated in the controller. And the idea of non-cooperative game was added [9], which provides a major support for the stable pointing technique of TGCS. However, the influence of road vibration of moving tank cannot be adequately. Realistic collisions between mechanical components, and vibration transfer processes are also ignored. Therefore, it is urgent to establish a dynamic model of TGCS considering various uncertainties and nonlinearities, which will be the first challenge and problem to be solved in this paper.

Secondly, as a servo control system, TGCS must ensure that the tank gun aims quickly, tracks stably and strikes accurately. The traditional control strategy cannot meet the needs of modern warfare. Over the past few decades, researchers have made many efforts to achieve this goal. In [10] and [11], based on the traditional PID controller, the control performance of the system is improved to a certain extent. However, PID is always a linear controller, and it is difficult to cope with the complex nonlinearities in TGCS, resulting in a sharp decrease in system performance. Furthermore, the adaptive nonlinear robust control method is applied to the TGCS control system [12], [13], [14], [15], [16], [17]. Specifically, Cai et al. effectively suppressed the parameter uncertainty and other uncertainties of the tank gun control system by using adaptive robust control strategy [12]. However, it only designs a nonlinear controller for the actuator of the TGCS system in essence, and does not consider the influence of the mechanical dynamics of the tank gun on the performance of the control system. Ma et al. designed an adaptive robust controller based on constraint following for the two-axis coupled dynamic model of TGCS [13]. On this basis, considering the coupling, nonlinearity and uncertainty of the tank gun, the nonlinear adaptive robust controller was applied to the moving TCGS system [14]. During the control of the tank gun, the barrel is brought close to the target angle if it deviates from the target and kept at the target angle if it is on the target. The adaptive robust control can ensure the system to obtain bounded stability, but its strong robustness is achieved by high-gain feedback, which is easy to stimulate the high-frequency dynamics not considered by the TGCS system and cause system instability. In order to further improve the control performance of the TGCS system, Li et al. designed an adaptive robust controller considering friction compensation [15]. At the same time, in order to reduce the influence of unmodeled disturbance on system tracking performance, the extended state observer and adaptive robust controller are combined to obtain excellent control effects [16]. In addition, Chen et al. [17] proposed a neural adaptive controller, which uses neural network to compensate for the uncertainty of tank vertical stability system, and the network weights and thresholds are adjusted online adaptively. Furthermore, Ma et al. [18] proposed an adaptive integral robust control strategy based on neural network, which can guarantee the asymptotic tracking performance of the TGCS system in the presence of uncertain nonlinearity. However, its controller design requires a strong assumption that the first and second derivatives of the system disturbance upper bound are continuous and differentiable. This is difficult to guarantee in complex TGCS systems, so it is not conducive to engineering applications. In addition, the above control strategy has also proved its effectiveness in a variety of other fields, such as robots [19], [20], [21], PMSM [22], [23], UAV [24], [25], [26], hydraulic actuators [27], [28], [29], [30] and new energy vehicles [31], [32]. However, the excellent control performance of these controllers is inevitably affected by the high gain feedback, and the experimental verification of the control strategy has not been completed for the actual TGCS system. In order to improve the stability of TGCS system effectively, a bold idea is generated. For the complex TGCS system, the adaptive technique is used to deal with the system parameter uncertainties, the dynamic compensation method based on neural network is used to reduce the influence of unmodeled dynamics and model uncertainties on the control performance, and the nonlinear robust control law is designed to enhance the robustness of the system. The effectiveness of the proposed method is verified by co-simulation and experiment.

Inspired by the above research, this paper firstly analyzes the influence of servo motor of tank gun actuator on the vibration characteristics of the system. The electromechanical coupling dynamic model considering the parameter uncertainty and uncertain nonlinearity for the bidirectional stability system of tank gun is established. Meanwhile, an adaptive robust control strategy based on neural network is designed by combining RBF neural network and adaptive method. The adaptive technology is applied to update unknown system parameters in real time to reduce the influence of parameter uncertainty on system stability, and a simple neural network is utilized to compensate the unknown dynamics of the bidirectional stability system, which is conducive to practical engineering application. Furthermore, a nonlinear robust feedback control law is constructed in the design of the control strategy, which further enhances the robustness of the proposed control strategy. The stability analysis based on Lyapunov function shows that the bounded stability performance can be obtained when there are various uncertainties in the system, which ensures the stability control of the tank gun in moving. The effectiveness of the proposed control strategy is verified by a large number of comparison results of co-simulation and experiments.

ABBREVIATIONS

TGCS	tank gun control system
PMSM	permanent magnet synchronous motor
ARC	adaptive robust control
RBFNN	radial basis function neural network

FOC field-oriented control
PID proportional integral differential
DSP digital signal processor
IPC industrial personal computer

The main contributions of this paper are as follows.

(1) A dynamics model of permanent magnet synchronous motor for tank bidirectional stability system is established considering uncertainty, and an adaptive robust controller based on RBFNN compensation is designed.

(2) Stability analysis shows that the proposed control strategy can obtain bounded stability performance even with various uncertainties.

(3) The process of co-simulation and semi-physical simulation actually simulated the moving environment of the tank, and a large number of comparison results verified the effectiveness of the proposed method.

The remaining sections of the paper are organized as follows. Section I introduces the mathematical dynamics model of PMSM and the nonlinear mathematical dynamics model of TGCS. In Section II, we design an ARC controller based on RBFNN compensation for the TGCS. Section III establishes the road roughness model, analyzes the connection relationships between the primary components of the entire tank, and develops the multibody dynamics model of the moving tank for co-simulation verification. In Section IV, we construct a semi-physical simulation platform based on DSP28335 to provide experimental verification. The stability proof of the designed controller based on Lyapunov theory [33] is presented in the Appendix

II. ELECTROMECHANICAL COUPLING DYNAMICS MODEL OF TGCS

A. MATHEMATICAL MODEL OF PMSM

The all-electric tank gun control system uses PMSMs as actuators to drive the horizontal and pitching movements of the gun. This is mainly due to the advantages of simple structure, high power density, outstanding control performance and fast dynamic response of the permanent magnet synchronous motor [34]. To facilitate the modelling of the dynamics of the PMSMs of TGCS, the parameters in a three-phase fixed coordinate system Oabc can be transformed into parameters in a synchronous rotating coordinate system Odq using the Clarke and Park transformations [35]. A coordinate system, as illustrated in Fig. 1, is established on top of the rotor. In this coordinate system, θ_e and ω_e represent the electrical angular displacement and angular velocity of the rotor, respectively.

By means of Clarke and Park transformations, we can obtain

$$\boldsymbol{f}_{dq} = \boldsymbol{T}_{dq-abc} \cdot \boldsymbol{f}_{abc}, \tag{1}$$

where

$$\boldsymbol{T}_{dq-abc} = \begin{bmatrix} \cos\theta_e & \cos\left(\theta_e - 2\pi/3\right) & \cos\left(\theta_e + 2\pi/3\right) \\ -\sin\theta_e & -\sin\left(\theta_e - 2\pi/3\right) & -\sin\left(\theta_e + 2\pi/3\right) \end{bmatrix},$$
$$\boldsymbol{f}_{abc} = [f_a, f_b, f_c]^{\mathrm{T}} \quad \text{and} \quad \boldsymbol{f}_{dq} = \left[f_d, f_q\right]^{\mathrm{T}}.$$

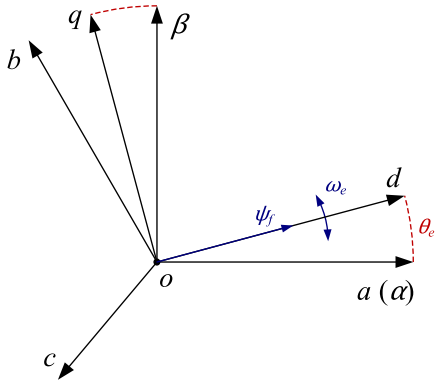

FIGURE 1. Phase diagram of PMSM.

TABLE 1. Meaning of the symbols in the PMSM.

symbol	meaning	symbol	meaning
u_d , u_q	stator voltage of d-q axis	T_e	Electromagnetic torque
i_d , i_q	Stator current of d-q axis	T_L	Load torque
ψ_{rd} ,	Stator flux of d-q axis	J_m	Rotor inertia
L_d , L_q	Stator inductor of d-q axis	R_s	Stator resistance
ψ_f	Rotor permanent magnet flux	B_m	Hysteresis coefficient
n_p	Number of magnetic pole pairs		

Indeed, $\boldsymbol{f}_{abc}$ and $\boldsymbol{f}_{dq}$ can represent voltages, currents, or other vectors in the three-phase fixed coordinate system Oabc. When applying the Clarke and Park transformation to convert these parameters into the synchronous rotating system Odq, these quantities preserve their physical meaning while simplifying mathematical analysis and control design for the PMSM system.

The mathematical model of the PMSM typically comprises the voltage equation, stator flux equation, electromagnetic torque equation, and mechanical motion equation. The meanings of the symbols used in the PMSM model are defined in Table 1. This comprehensive representation of the PMSM allows for a thorough understanding of its behavior under various operating conditions and facilitates the development of advanced control strategies to optimize its performance in diverse applications.

The aforementioned equations can be reformulated in the Odq coordinate system as follows. This transformation simplifies the mathematical representation and analysis of the PMSM system, which in turn makes it easier to develop and implement control strategies for improved performance and efficiency under various operating conditions. That is

$$\begin{cases} u_d = R_s i_d - \omega_e L_q i_q + L_d \dfrac{\mathrm{d}i_d}{\mathrm{d}t} \\ u_q = \omega_e L_d i_d + R_s i_q + L_q \dfrac{\mathrm{d}i_q}{\mathrm{d}t} + \omega_e \psi_f. \end{cases} \tag{2}$$

Voltage equation simplifies the mathematical representation and analysis of the PMSM system, which in turn makes

it easier to develop and implement control strategies for improved performance and efficiency under various operating conditions. Furthermore, the relationship between the stator flux and the stator current can be expressed as

$$\begin{cases} \psi_{rd} = L_d i_d + \psi_f \\ \psi_{rq} = L_q i_q. \end{cases} \tag{3}$$

Then the electromagnetic torque equation can be described as

$$T_e = \frac{3}{2} n_p \left[\psi_f i_q + \left(L_d - L_q \right) i_d i_q \right]. \tag{4}$$

Considering the mechanical characteristics of the tank gun and the electrical characteristics of the actuator, its electromechanical coupling dynamics is modelled as

$$T_e - T_L = \frac{B_m}{n_p} \omega_e + \frac{J_m}{n_p} \cdot \frac{\mathrm{d}\omega_e}{\mathrm{d}t} \tag{5}$$

Here, let ω_m be the mechanical angular velocity of the PMSM $\omega_e = n_p \omega_m$, then, equation (5) can be rewritten as

$$T_e - T_L = B_m \omega_m + J_m \dot{\omega}_m. \tag{6}$$

Remark 1: As demonstrated in equation (3), the electromagnetic torque is dependent on the rotor permanent magnet's magnetic flux ψ_f and the stator currents i_d and i_q. Given that the magnetic flux ψ_f remains constant, the electromagnetic output torque of the PMSM can be modulated by adjusting i_d and i_q. This capability can precisely ensure the torque output of the tank gun control system and guarantee the precise and stable control of the tank gun.

However, the electromagnetic torque cannot be directly controlled by adjusting the current due to the nonlinearity and coupling between the currents i_d and i_q in the PMSM. To enhance the control performance of the system, the field-oriented control (FOC) scheme is introduced [36]. In this manner, the control process of the PMSM drive system is simplified, resembling that of a DC motor [37]. Consequently, the voltage equation and the electromagnetic torque equation can be reformulated as

$$\begin{cases} u_d = -\omega_e L_q i_q \\ u_q = R_s i_q + L_q \dfrac{\mathrm{d}i_q}{\mathrm{d}t} + \omega_e \psi_f \end{cases} \tag{7}$$

and

$$T_e = \frac{3}{2} n_p \psi_f i_q = K_T i_q, \tag{8}$$

where $K_T := \frac{3}{2} n_p \psi_f$ denotes the electromagnetic torque coefficient.

Remark 2: The FOC implementation based on $i_d^* = 0$ is shown in Fig. 2. The actual speed of the motor rotor detected by the encoder is compared with the control commands. The reference current i_q^* for the q-axis is output by the controller. The current sensor takes measurements of the three-phase stator currents i_a, i_b, i_c, and obtains the stator currents i_d and i_q by coordinate transformation. After comparing the reference currents i_d^* and i_q^* with the actual currents i_d and i_q, the $d-q$ axis reference voltages u_d^* and u_q^* of can be calculated using a current controller. Then, the reference voltages u_α^* and u_β^* for the α-axis and β-axis can be calculated using the In-Park transform. The control signal for PWM output is produced based on the Space Vector Pulse Width Modulation (SVPWM) method, ultimately resulting in the inverter delivering three-phase currents to govern the motion of the PMSM. This sequence forms a closed-loop control system.

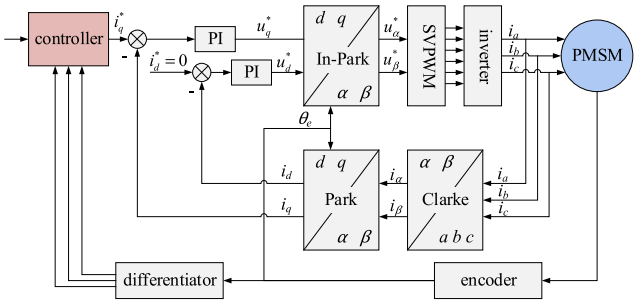

FIGURE 2. FOC implementation principle.

B. MATHEMATICAL DYNAMICS MODEL OF TGCS

The structure of the bidirectional stability control system of the all-electric tank gun is shown in Fig. 3. The PMSM is used to drive the turret rotation in the azimuth direction and the electric cylinder is used to drive the gun rotation in the elevation direction. Their principle is essentially the same, under the action of the controller PMSM through the reducer to generate driving torque to drive the turret and gun movement.

In this paper, we take the vertical control subsystem as an example and give a schematic diagram of its specific working principle as shown in Fig. 4.

As the TGCS uses the similar PMSM for the motor in the horizontal direction and the electric cylinder in the vertical direction, they are modelled theoretically in a similar way. In the presentation below, the subscript $\cdot_h$ indicates the horizontal system and the subscript $\cdot_v$ indicates the vertical system. The rotation angle of the tank muzzle is not linearly related to the speed of the motor, due to the presence of nonlinearities and uncertainties in TGCS. To facilitate the description and establishment of the transmission model, an approximate reduction ratio $\boldsymbol{n} = [n_h, n_v]$ is assumed to exist between them. It can be written as

$$\begin{cases} \boldsymbol{\omega}_m = \boldsymbol{n} \circ (\boldsymbol{\omega} + \Delta\boldsymbol{\omega}) \\ \boldsymbol{T} = \boldsymbol{n} \circ (\boldsymbol{T}_L + \Delta\boldsymbol{T}_L), \end{cases} \tag{9}$$

where $\boldsymbol{T}_L = [T_{hL}, T_{vL}]$ is the output torque of the motor, $\boldsymbol{T} = [T_h, T_v]$ is the drive torque of the motor converted to the center of rotation, $\boldsymbol{\omega}_m = [\omega_{hm}, \omega_{vm}]$ is the output speed of the motor, and $\boldsymbol{\omega} = [\omega_h, \omega_v]$ is the angular velocity of the tank muzzle movement in the controlled direction. $\Delta\boldsymbol{\omega} = [\Delta\omega_h, \Delta\omega_v]$ and $\Delta\boldsymbol{T}_L = [\Delta T_{hL}, \Delta T_{vL}]$ denote the transmission errors of $\boldsymbol{\omega}$ and $\boldsymbol{T}_L$ respectively.

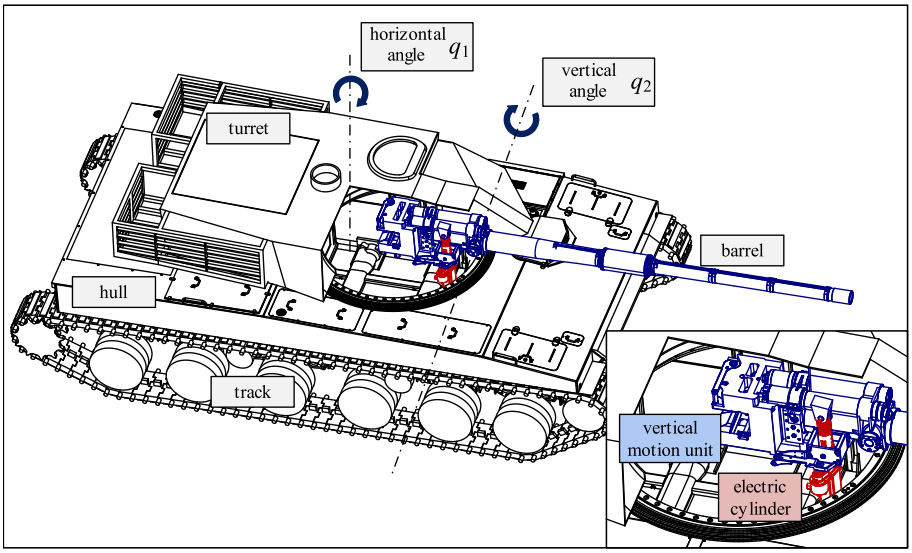

FIGURE 3. All-electric tank stabilization device.

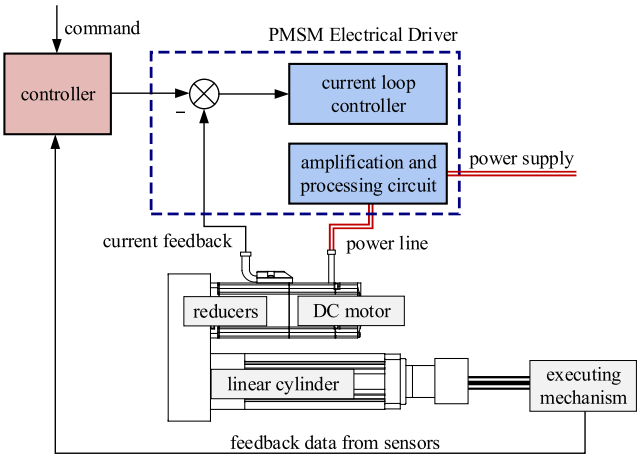

FIGURE 4. PMSM servo system of all-electric tank in vertical direction.

Remark 3.1: Let $\boldsymbol{A}, \boldsymbol{B} \in \mathbb{C}^{m\times n}$ with $\boldsymbol{A} = \{a_{ij}\}$ and $\boldsymbol{B} = \{b_{ij}\}$, then the $m \times n$ matrix

$$\boldsymbol{U} = \begin{bmatrix} a_{11}b_{11} & a_{12}b_{12} & \cdots & a_{1n}b_{1n} \\ a_{21}b_{21} & a_{22}b_{22} & \cdots & a_{2n}b_{2n} \\ \vdots & \vdots & & \vdots \\ a_{m1}b_{11} & a_{m2}b_{m2} & \cdots & a_{mn}b_{mn} \end{bmatrix} \tag{10}$$

is defined as the Hadamard product of $\boldsymbol{A}$ and $\boldsymbol{B}$, denoted as $\boldsymbol{U} = \boldsymbol{A} \circ \boldsymbol{B}$.

*Remark 3.2:*Let $\boldsymbol{C}, \boldsymbol{D} \in \mathbb{C}^{m\times n}$ with $\boldsymbol{C} = \{c_{ij}\}$ and $\boldsymbol{D} = \{d_{ij}\}$. If it is satisfied that

$$c_{ij} \neq 0, d_{ij} \neq 0, c_{ij}d_{ij} = 1, \tag{11}$$

then we denote $\boldsymbol{D} = \boldsymbol{C}^{\ominus}$ and $\boldsymbol{C} = \boldsymbol{D}^{\ominus}$ for ease of description.

Taking equations (9) and (8) into equation(7), we get

$$\begin{aligned} \boldsymbol{J}_m \circ \boldsymbol{n} \circ (\dot{\boldsymbol{\omega}} + \Delta\dot{\boldsymbol{\omega}}) = \boldsymbol{K}_T \circ \boldsymbol{i}_q - \boldsymbol{B}_m \circ \boldsymbol{n} \circ (\boldsymbol{\omega} + \Delta\boldsymbol{\omega}) \\ - \boldsymbol{T} \circ \boldsymbol{n}^{\ominus} - \Delta\boldsymbol{T}_L, \end{aligned} \tag{12}$$

where $\boldsymbol{J}_m = [J_{hm}, J_{vm}]$ denotes the rotor inertia of the motor with the tank in the bidirectional direction, $\boldsymbol{K}_T = [K_{hT}, K_{vT}]$ denotes the torque coefficient, $\boldsymbol{B}_m = [B_{hm}, B_{vm}]$ is the corresponding hysteresis coefficient, $\boldsymbol{i}_q = [i_{hq}, i_{vq}]$ is the corresponding q-axis current. $\boldsymbol{q} = [q_h, q_v]$ denotes the rotation angle of the muzzle in the controlled direction and can be rewritten as

$$\begin{aligned} \boldsymbol{n} \circ \boldsymbol{J}_m \circ \dot{\boldsymbol{\omega}} = \boldsymbol{K}_T \circ \boldsymbol{i}_q - \boldsymbol{n} \circ \boldsymbol{B}_m \circ \boldsymbol{\omega} - \boldsymbol{T} \circ \boldsymbol{n}^{\ominus} \\ - (\boldsymbol{n} \circ \boldsymbol{J}_m \circ \Delta\dot{\boldsymbol{\omega}} + \boldsymbol{n} \circ \boldsymbol{B}_m \circ \Delta\boldsymbol{\omega} + \Delta\boldsymbol{T}_L). \end{aligned} \tag{13}$$

Further, let $\boldsymbol{J}_{\text{equ}} = [J_{h\text{equ}}, J_{v\text{equ}}] = \boldsymbol{n} \circ \boldsymbol{J}_m$, $\boldsymbol{B}_{\text{equ}} = [B_{h\text{equ}}, B_{v\text{equ}}] = \boldsymbol{n} \circ \boldsymbol{B}_m$, $\boldsymbol{d}_n = [d_{hn}, d_{vn}] = \boldsymbol{T} \circ \boldsymbol{n}^{\ominus}$. And to improve the accuracy of the controller, $\boldsymbol{\tau}_d = [\tau_{hd}, \tau_{vd}]$ is introduced to denote the modeling error and other uncompensated disturbances, such as nonlinear friction, external disturbances. The above equation continues to be rewritten as

$$\boldsymbol{J}_{\text{equ}} \circ \ddot{\boldsymbol{q}} = \boldsymbol{K}_T \circ \boldsymbol{i}_q - \boldsymbol{B}_{\text{equ}} \circ \dot{\boldsymbol{q}} - \boldsymbol{d}_n - \boldsymbol{\tau}_d. \tag{14}$$

*Remark 4:*To facilitate the design of the controller, the following assumptions are made.

(1) The upper and lower limits of all system parameters are known, providing a well-defined range within which the system operates. This knowledge facilitates effective analysis, control design, and optimization of the system performance, ensuring it functions efficiently and reliably under various conditions while

maintaining its operational constraints. That is

$$\begin{aligned} &\left\|J_{1equ}\right\| \leq \kappa_1, \quad \|K_{1T}\| \leq \kappa_2, \quad \left\|B_{1\mathrm{equ}}\right\| \leq \kappa_3, \\ &\|d_{1n}\| \leq \kappa_4, \quad \left\|J_{2equ}\right\| \leq \kappa_5, \quad \|K_{2T}\| \leq \kappa_6, \\ &\left\|B_{2\mathrm{equ}}\right\| \leq \kappa_7, \quad \|d_{2n}\| \leq \kappa_8 \end{aligned} \tag{15}$$

where κ_1, κ_2, κ_3, κ_4, κ_5, κ_6, κ_7, κ_8 are positive real numbers of known finite size.

(2) Although $\boldsymbol{\tau}_d$ is an unknown quantity that varies with time, it is bounded, meaning it has an upper and lower limit within a specific range. This constraint helps in simplifying the analysis and control of dynamic systems, as it ensures that the variable remains within a predictable range despite its time-varying nature. That is

$$\|\tau_{1d}\| \leq \vartheta_1, \quad \|\tau_{2d}\| \leq \vartheta_2, \tag{16}$$

where ϑ_1 and ϑ_2 are positive real numbers of unknown finite size.

In reality, obtaining the exact values of all system parameters is often not feasible. Consequently, the primary system parameters considered in the paper may slowly change over time in real-world conditions. To mitigate the impact of these parameter uncertainties and enhance system performance, the state space equations' parameters are linearized using an adaptive method. This parameter adaptation approach allows for better tracking and compensation of variations, resulting in improved control accuracy and robustness in dynamic environments. A parameter vector is defined to represent the key system parameters as

$$\Theta = [\boldsymbol{\theta}_1, \boldsymbol{\theta}_2, \boldsymbol{\theta}_3]^{\mathrm{T}} = \begin{bmatrix} \theta_{h1} & \theta_{v1} \\ \theta_{h2} & \theta_{v2} \\ \theta_{h3} & \theta_{v3} \end{bmatrix} = \begin{bmatrix} \boldsymbol{J}_{\mathrm{equ}} \circ \boldsymbol{K}_T^{\ominus} \\ \boldsymbol{B}_{\mathrm{equ}} \circ \boldsymbol{K}_T^{\ominus} \\ \boldsymbol{d}_n \circ \boldsymbol{K}_T^{\ominus} \end{bmatrix}. \tag{17}$$

Rewriting equation (14), one gets

$$\boldsymbol{\theta}_1 \circ \ddot{\boldsymbol{q}} = \boldsymbol{i}_q - \boldsymbol{\theta}_2 \circ \dot{\boldsymbol{q}} - \boldsymbol{\theta}_3 - \boldsymbol{\tau}_{d1}, \tag{18}$$

where $\boldsymbol{\tau}_{d'} = \boldsymbol{\tau}_d \circ \boldsymbol{K}_T^{-1} = [\tau_{hd'}, \tau_{vd'}]$. The system state space equations of TGCS can be described as

$$\begin{aligned} \dot{\boldsymbol{x}}_1 &= \boldsymbol{x}_2 \\ \boldsymbol{\theta}_1 \circ \dot{\boldsymbol{x}}_2 &= \boldsymbol{i}_q - \boldsymbol{\theta}_2 \circ \boldsymbol{x}_2 - \boldsymbol{\theta}_3 - \boldsymbol{\tau}_{d'} \\ \boldsymbol{y} &= \boldsymbol{x}_1, \end{aligned} \tag{19}$$

where $\boldsymbol{X} = [\boldsymbol{x}_1, \boldsymbol{x}_2]^{\mathrm{T}} = [\boldsymbol{y}, \dot{\boldsymbol{y}}]^{\mathrm{T}}$ denotes the bidirectional stability system state. Based on the above assumptions, we can obtain

$$\Theta \in \Omega_\Theta = \{\Theta : \Theta_{\min} < \Theta < \Theta_{\max}\} \tag{20}$$

and

$$\|\boldsymbol{\tau}_{d'}\| \leq \delta_d. \tag{21}$$

where $\Theta_{\min} = [\boldsymbol{\theta}_{1\min}, \boldsymbol{\theta}_{2\min}, \boldsymbol{\theta}_{3\min}]^{\mathrm{T}}$ and $\Theta_{\max} = [\boldsymbol{\theta}_{1\max}, \boldsymbol{\theta}_{2\max}, \boldsymbol{\theta}_{3\max}]^{\mathrm{T}}$ are the upper and lower bounds of $\boldsymbol{\theta}_1$, $\boldsymbol{\theta}_2$, $\boldsymbol{\theta}_3$, respectively, and δ_d is a real number of known finite size.

III. TANK BIDIRECTIONAL STABILIZATION CONTROLLER

A. TORQUE-BASED CONTROLLER DESIGN

Step 1: The position tracking error is defined as $\boldsymbol{\alpha}_1 = \boldsymbol{x}_1 - \boldsymbol{x}_{1\mathrm{d}}$, with $\boldsymbol{x}_{1\mathrm{d}}$ denoting the desired position. Taking the derivative of $\boldsymbol{\alpha}_1$ yields

$$\dot{\boldsymbol{\alpha}}_1 = \dot{\boldsymbol{x}}_1 - \dot{\boldsymbol{x}}_{1\mathrm{d}} = \boldsymbol{x}_2 - \dot{\boldsymbol{x}}_{1\mathrm{d}}. \tag{22}$$

We design $\boldsymbol{x}_{2\mathrm{eq}}$ as a virtual control rate for state $\boldsymbol{x}_2$, which is used to guarantee the output tracking performance. Defining $\boldsymbol{\alpha}_2 = \boldsymbol{x}_2 - \boldsymbol{x}_{2\mathrm{eq}}$ as the deviation between them, combining with equation (22) yields

$$\dot{\boldsymbol{\alpha}}_1 = \boldsymbol{\alpha}_2 + \boldsymbol{x}_{2\mathrm{eq}} - \dot{\boldsymbol{x}}_{1\mathrm{d}}. \tag{23}$$

Here, $\boldsymbol{x}_{2\mathrm{eq}}$ is designed as $\boldsymbol{x}_{2\mathrm{eq}} = \dot{\boldsymbol{x}}_{1\mathrm{d}} - \boldsymbol{k}_1 \circ \boldsymbol{\alpha}_1$, and $\boldsymbol{k}_1$ is the positive robust feedback gain. Equation (23) can be rewritten as

$$\dot{\boldsymbol{\alpha}}_1 = \boldsymbol{\alpha}_2 - \boldsymbol{k}_1 \circ \boldsymbol{\alpha}_1. \tag{24}$$

Evidently, $\dot{\boldsymbol{\alpha}}_1$ can converge to zero as long as $\boldsymbol{\alpha}_2$ is made to converge to zero.

Step 2: In Step 1, the robust virtual control rate $\boldsymbol{x}_{2\mathrm{eq}}$ is accomplished, and in this step the actual control rate will be determined for $\boldsymbol{i}_q$. Combining (15) and deriving for $\dot{\boldsymbol{\alpha}}_2$ yields

$$\begin{aligned} \boldsymbol{\theta}_1 \circ \dot{\boldsymbol{\alpha}}_2 &= \boldsymbol{\theta}_1 \circ \dot{\boldsymbol{x}}_2 - \boldsymbol{\theta}_1 \circ \dot{\boldsymbol{x}}_{2\mathrm{eq}} \\ &= \boldsymbol{i}_q - \boldsymbol{\theta}_2 \circ \boldsymbol{x}_2 - \boldsymbol{\theta}_3 - \boldsymbol{\tau}_{d'} - \boldsymbol{\theta}_1 \circ \dot{\boldsymbol{x}}_{2\mathrm{eq}}. \end{aligned} \tag{25}$$

From the above, the following controller is designed

$$\begin{cases} \boldsymbol{i}_q = \boldsymbol{i}_{\mathrm{s}} + \boldsymbol{i}_{\mathrm{a}} \\ \boldsymbol{i}_{\mathrm{a}} = \hat{\boldsymbol{\theta}}_1 \circ \dot{\boldsymbol{x}}_{2\mathrm{eq}} + \hat{\boldsymbol{\theta}}_2 \circ \boldsymbol{x}_2 + \hat{\boldsymbol{\theta}}_3 + \hat{\boldsymbol{\tau}}_{d'} \\ \boldsymbol{i}_{\mathrm{s}} = \boldsymbol{i}_{\mathrm{s1}} + \boldsymbol{i}_{\mathrm{s2}} \\ \boldsymbol{i}_{\mathrm{s1}} = -\boldsymbol{k}_2 \circ \boldsymbol{\alpha}_2, \end{cases} \tag{26}$$

where $\boldsymbol{i}_{\mathrm{a}}$ is the feedforward compensation term of the system adaptive model, $\boldsymbol{i}_{\mathrm{s1}}$ is the linear robust feedback term, and $\boldsymbol{k}_2$ is the positive robust feedback gain. Errors in parameter estimation and disturbance estimation are compensated utilized by $\boldsymbol{i}_{\mathrm{s2}}$. The system will be made stable by design $\boldsymbol{i}_{\mathrm{s2}}$ in Step 3. $\hat{\Theta} = \left[\hat{\boldsymbol{\theta}}_1, \hat{\boldsymbol{\theta}}_2, \hat{\boldsymbol{\theta}}_3\right]^{\mathrm{T}}$ is the estimate of $\Theta = [\boldsymbol{\theta}_1, \boldsymbol{\theta}_2, \boldsymbol{\theta}_3]^{\mathrm{T}}$ and $\hat{\tau}_{d'}$ is the estimate of $\tau_{d'}$. Bringing equation (26) into equation (25) yields

$$\begin{aligned} \boldsymbol{\theta}_1 \dot{z}_2 &= \hat{\boldsymbol{\theta}}_1 \circ \dot{\boldsymbol{x}}_{2\mathrm{eq}} + \hat{\boldsymbol{\theta}}_2 \circ \boldsymbol{x}_2 + \hat{\boldsymbol{\theta}}_3 + \hat{\boldsymbol{\tau}}_{d'} + \boldsymbol{i}_{\mathrm{s2}} - \boldsymbol{k}_2 \circ \boldsymbol{\alpha}_2 \\ &\quad - \boldsymbol{\theta}_2 \circ \boldsymbol{x}_2 - \boldsymbol{\theta}_3 - \boldsymbol{\tau}_{d'} - \boldsymbol{\theta}_1 \circ \dot{\boldsymbol{x}}_{2\mathrm{eq}} \\ &= \dot{\boldsymbol{x}}_{2\mathrm{eq}} \circ \left(\hat{\boldsymbol{\theta}}_1 - \boldsymbol{\theta}_1\right) + \boldsymbol{x}_2 \circ \left(\hat{\boldsymbol{\theta}}_2 - \boldsymbol{\theta}_2\right) + \left(\hat{\boldsymbol{\theta}}_3 - \boldsymbol{\theta}_3\right) \\ &\quad + \left(\hat{\boldsymbol{\tau}}_{d'} - \boldsymbol{\tau}_{d'}\right) + \boldsymbol{i}_{\mathrm{s2}} - \boldsymbol{k}_2 \circ \boldsymbol{\alpha}_2. \end{aligned} \tag{27}$$

Define $\tilde{\Theta} = \hat{\Theta} - \Theta = \left[\hat{\boldsymbol{\theta}}_1 - \boldsymbol{\theta}_1, \hat{\boldsymbol{\theta}}_2 - \boldsymbol{\theta}_2, \hat{\boldsymbol{\theta}}_3 - \boldsymbol{\theta}_3\right]^{\mathrm{T}}$ as the estimation error of Θ, $\Phi = \left[-\dot{\boldsymbol{x}}_{2\mathrm{eq}}, -\boldsymbol{x}_2, -\boldsymbol{\varphi}\right]^{\mathrm{T}}$ as the regressor, $\boldsymbol{\varphi} = [1, 1]$, and $\tilde{\boldsymbol{\tau}}_{d'} = \hat{\boldsymbol{\tau}}_{d'} - \boldsymbol{\tau}_{d'}$ as the estimation error of $\tau_{d'}$. Equation (23) can be rewritten as

$$\boldsymbol{\theta}_1 \circ \dot{\boldsymbol{\alpha}}_2 = -\boldsymbol{k}_2 \circ \boldsymbol{\alpha}_2 - \Phi^{\mathrm{T}} \circ \tilde{\Theta} + \hat{\boldsymbol{\tau}}_{d'} - \boldsymbol{\tau}_{d'} + \boldsymbol{i}_{\mathrm{s2}}. \tag{28}$$

B. RBFNN-BASED DISTURBANCE COMPENSATION

The ARC serves as an efficient approach for estimating indeterminate system parameters in the presence of uncertainties. As nonlinear disturbances escalate, uncertainty noise magnification may lead to system instability. Given the remarkable approximation competencies of RBFNNs, their incorporation for assessing all unidentified disturbances proves advantageous. The driving signal relies on a linear blend of tracking and weight estimation errors for parameter appraisal and structural uncertainty error estimation. By integrating the merits of these techniques, a novel control scheme is established. Depicted in Fig. 5, this innovative control strategy's schematic representation is illustrated.

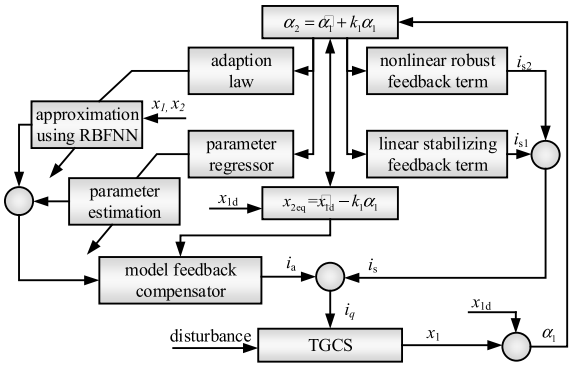

FIGURE 5. Structure of the proposed controller.

Step 3: RBFNN are capable of approximating smooth nonlinear functions with any desired level of accuracy. In this step, we designed a RBFNN observer to estimate the uncertainties and some unknown disturbances in TGCS. The neural network for training it is shown in Fig. 6.

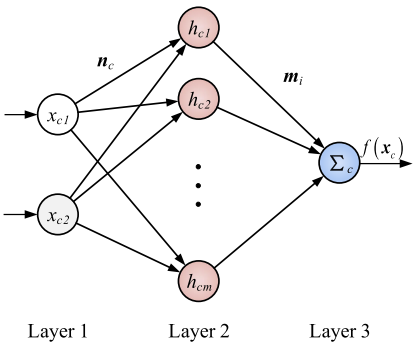

FIGURE 6. The principle framework of RBFNN.

The RBF neural network output $f(\boldsymbol{X})$, which represents the error compensation quantity $\boldsymbol{\tau}_{d'}$, is designed as

$$f(\boldsymbol{X}) = \boldsymbol{M}^{\mathrm{T}} \circ \sigma\left(\boldsymbol{N}^{\mathrm{T}} \circ \boldsymbol{X}\right) - \boldsymbol{\varepsilon}_{\mathrm{approx}} = \boldsymbol{\tau}_{d'}, \tag{29}$$

where $\sigma(z)$ is a nonlinear function, which has the expression

$$\sigma(z) = \frac{1 - e^{-az}}{1 + e^{-az}}. \tag{30}$$

$\boldsymbol{X} = [\boldsymbol{x}_h, \boldsymbol{x}_v]^{\mathrm{T}}$ denotes the input to the network. $\boldsymbol{\varepsilon}_{\mathrm{approx}} = \left[\varepsilon_{h\mathrm{approx}}, \varepsilon_{v\mathrm{approx}}\right]$ denotes the error of the network's approximation. $\boldsymbol{M} = [\boldsymbol{m}_h, \boldsymbol{m}_v]$ and $\boldsymbol{N} = [\boldsymbol{n}_h, \boldsymbol{n}_v]$ are the ideal weights of the network that minimize the value of $\left|\varepsilon_{h\mathrm{approx}}\right|$ and $\left|\varepsilon_{v\mathrm{approx}}\right|$. $\hat{\boldsymbol{M}} = \left[\hat{\boldsymbol{m}}_h, \hat{\boldsymbol{m}}_v\right]$ and $\hat{\boldsymbol{N}} = \left[\hat{\boldsymbol{n}}_h, \hat{\boldsymbol{n}}_v\right]$ are defined as the estimations of $\boldsymbol{M}$ and $\boldsymbol{N}$, respectively.

The estimated output $\hat{f}(\boldsymbol{X})$ of the output network is obtained as

$$\hat{f}(\boldsymbol{X}) = \hat{\boldsymbol{M}}^{\mathrm{T}} \circ \sigma\left(\hat{\boldsymbol{N}}^{\mathrm{T}} \circ \boldsymbol{X}\right) = \hat{\boldsymbol{\tau}}_{d'}. \tag{31}$$

Taking equation (31) and equation (29) into (28), we can obtain

$$\begin{aligned}\boldsymbol{\theta}_1 \circ \dot{\boldsymbol{\alpha}}_2 = &-\boldsymbol{k}_2 \circ \boldsymbol{\alpha}_2 - \Phi^{\mathrm{T}} \circ \tilde{\Theta} + \hat{\boldsymbol{M}}^{\mathrm{T}} \circ \sigma\left(\hat{\boldsymbol{N}}^{\mathrm{T}} \circ \boldsymbol{X}\right) \\ &- \boldsymbol{M}^{\mathrm{T}} \circ \sigma\left(\boldsymbol{N}^{\mathrm{T}} \circ \boldsymbol{X}\right) + \boldsymbol{\varepsilon}_{\mathrm{approx}} + \boldsymbol{i}_{s2}.\end{aligned} \tag{32}$$

Define $\tilde{\boldsymbol{M}} = \hat{\boldsymbol{M}} - \boldsymbol{M} = \left[\tilde{\boldsymbol{m}}_v, \tilde{\boldsymbol{m}}_h\right]$ and $\tilde{\boldsymbol{N}} = \hat{\boldsymbol{N}} - \boldsymbol{N} = \left[\tilde{\boldsymbol{n}}_v, \tilde{\boldsymbol{n}}_h\right]$ as the estimation errors of the ideal weights. The Taylor expansion of the function $\sigma\left(\boldsymbol{N}^{\mathrm{T}} \circ \boldsymbol{X}\right)$ at $\boldsymbol{N}^{\mathrm{T}} \circ \boldsymbol{X} = \hat{\boldsymbol{N}}^{\mathrm{T}} \circ \boldsymbol{X}$ can be written as

$$\begin{aligned}&\sigma\left(\boldsymbol{N}^{\mathrm{T}} \circ \boldsymbol{X}\right) \\ &= \sigma\left(\hat{\boldsymbol{N}}^{\mathrm{T}} \circ \boldsymbol{X}\right) + \sigma'\left(\hat{\boldsymbol{N}}^{\mathrm{T}} \circ \boldsymbol{X}\right)\left(\boldsymbol{N}^{\mathrm{T}} \circ \boldsymbol{X} - \hat{\boldsymbol{N}}^{\mathrm{T}} \circ \boldsymbol{X}\right) \\ &\quad + o\left(\boldsymbol{N}^{\mathrm{T}} \circ \boldsymbol{X} - \hat{\boldsymbol{N}}^{\mathrm{T}} \circ \boldsymbol{X}\right) \\ &= \sigma\left(\hat{\boldsymbol{N}}^{\mathrm{T}} \circ \boldsymbol{X}\right) - \sigma'\left(\hat{\boldsymbol{N}}^{\mathrm{T}} \circ \boldsymbol{X}\right)\tilde{\boldsymbol{N}}^{\mathrm{T}} \circ \boldsymbol{X} \\ &\quad + o\left(-\tilde{\boldsymbol{N}}^{\mathrm{T}} \circ \boldsymbol{X}\right),\end{aligned} \tag{33}$$

where $\sigma'\left(\boldsymbol{N}^{\mathrm{T}} \circ \boldsymbol{X}\right)$ is the Jacobi equation for $\sigma\left(\boldsymbol{N}^{\mathrm{T}} \circ \boldsymbol{X}\right)$. $o\left(\boldsymbol{N}^{\mathrm{T}} \circ \boldsymbol{X}\right)$ is the Peyano remainder term in the Taylor expansion, which is a higher order infinitesimal quantity. For the purpose of the following description, define $\hat{\boldsymbol{\sigma}} = \left[\hat{\sigma}_h, \hat{\sigma}_v\right] = \sigma\left(\hat{\boldsymbol{N}}^{\mathrm{T}} \circ \boldsymbol{X}\right)$, $\boldsymbol{\sigma'} = \left[\sigma'_h, \sigma'_v\right] = \sigma'\left(\boldsymbol{N}^{\mathrm{T}} \circ \boldsymbol{X}\right)$, $\hat{\boldsymbol{\sigma}}' = \left[\hat{\sigma}'_h, \hat{\sigma}'_v\right] = \sigma'\left(\hat{\boldsymbol{N}}^{\mathrm{T}} \circ \boldsymbol{X}\right)$. Rewriting equation (33), one obtains

$$\sigma\left(\boldsymbol{N}^{\mathrm{T}} \circ \boldsymbol{X}\right) = \hat{\boldsymbol{\sigma}} - \hat{\boldsymbol{\sigma}'} \circ \tilde{\boldsymbol{N}}^{\mathrm{T}} \circ \boldsymbol{X} + o\left(-\tilde{\boldsymbol{N}}^{\mathrm{T}} \circ \boldsymbol{X}\right). \tag{34}$$

The term $\hat{\boldsymbol{M}}^{\mathrm{T}} \circ \sigma\left(\hat{\boldsymbol{N}}^{\mathrm{T}} \circ \boldsymbol{X}\right) - \boldsymbol{M}^{\mathrm{T}} \circ \sigma\left(\boldsymbol{N}^{\mathrm{T}} \circ \boldsymbol{X}\right)$ in equation (32) can be written as

$$\begin{aligned}&\hat{\boldsymbol{M}}^{\mathrm{T}} \circ \sigma\left(\hat{\boldsymbol{N}}^{\mathrm{T}} \circ \boldsymbol{X}\right) - \boldsymbol{M}^{\mathrm{T}} \circ \sigma\left(\boldsymbol{N}^{\mathrm{T}} \circ \boldsymbol{X}\right) \\ &= \hat{\boldsymbol{M}}^{\mathrm{T}} \circ \hat{\boldsymbol{\sigma}} - \boldsymbol{M}^{\mathrm{T}} \circ \hat{\boldsymbol{\sigma}} + \boldsymbol{M}^{\mathrm{T}} \circ \hat{\boldsymbol{\sigma}}' \circ \tilde{\boldsymbol{N}}^{\mathrm{T}} \circ \boldsymbol{X} \\ &\quad - \boldsymbol{M}^{\mathrm{T}} \circ o\left(-\hat{\boldsymbol{N}}^{\mathrm{T}} \boldsymbol{X}\right) \\ &= \tilde{\boldsymbol{M}}^{\mathrm{T}} \circ \hat{\boldsymbol{\sigma}} + \boldsymbol{M}^{\mathrm{T}} \circ \hat{\boldsymbol{\sigma}}' \circ \tilde{\boldsymbol{N}}^{\mathrm{T}} \circ \boldsymbol{X} \\ &\quad - \boldsymbol{M}^{\mathrm{T}} \circ o\left(-\hat{\boldsymbol{N}}^{\mathrm{T}} \boldsymbol{X}\right) \\ &= \tilde{\boldsymbol{M}}^{\mathrm{T}} \circ \hat{\boldsymbol{\sigma}} + \left(\hat{\boldsymbol{M}}^{\mathrm{T}} - \tilde{\boldsymbol{M}}^{\mathrm{T}}\right) \circ \hat{\boldsymbol{\sigma}}' \circ \tilde{\boldsymbol{N}}^{\mathrm{T}} \circ \boldsymbol{X} \\ &\quad - \boldsymbol{M}^{\mathrm{T}} \circ o\left(-\hat{\boldsymbol{N}}^{\mathrm{T}} \boldsymbol{X}\right) \\ &= \tilde{\boldsymbol{M}}^{\mathrm{T}} \circ \left(\hat{\boldsymbol{\sigma}} - \hat{\boldsymbol{\sigma}}' \circ \tilde{\boldsymbol{N}}^{\mathrm{T}} \circ \boldsymbol{X}\right) + \hat{\boldsymbol{M}}^{\mathrm{T}} \circ \hat{\boldsymbol{\sigma}}' \circ \tilde{\boldsymbol{N}}^{\mathrm{T}} \circ \boldsymbol{X} \\ &\quad - \boldsymbol{M}^{\mathrm{T}} \circ o\left(-\hat{\boldsymbol{N}}^{\mathrm{T}} \boldsymbol{X}\right).\end{aligned} \tag{35}$$

Defining $\boldsymbol{\omega} = [\omega_h, \omega_v] = -\boldsymbol{M}^{\mathrm{T}} \circ o\left(-\hat{\boldsymbol{N}}^{\mathrm{T}} \circ \boldsymbol{X}\right) = \left[-\boldsymbol{m}_h^{\mathrm{T}} \cdot o\left(-\hat{\boldsymbol{n}}_h^{\mathrm{T}} \boldsymbol{x}_h\right), -\boldsymbol{m}_v^{\mathrm{T}} \cdot o\left(-\hat{\boldsymbol{n}}_v^{\mathrm{T}} \boldsymbol{x}_v\right)\right]$, based on the above derivation, we have

$$\begin{aligned} |\omega_c| &\leq \|\boldsymbol{n}_c\|_{\mathrm{F}} \left\|\boldsymbol{x}_c \hat{\boldsymbol{m}}_c^{\mathrm{T}} \hat{\boldsymbol{\sigma}}'_c\right\|_{\mathrm{F}} + \|\boldsymbol{m}_c\| \cdot \left\|\hat{\boldsymbol{\sigma}}'_c \hat{\boldsymbol{n}}_c^{\mathrm{T}} \boldsymbol{x}_c\right\| + \|\boldsymbol{m}_c\|_1 \\ &\leq \max\left\{\|\boldsymbol{n}_c\|_{\mathrm{F}}, \|\boldsymbol{m}_c\|, \|\boldsymbol{m}_c\|_1\right\} \\ &\quad \cdot \left(\left\|\boldsymbol{x}_c \hat{\boldsymbol{m}}_c^{\mathrm{T}} \hat{\boldsymbol{\sigma}}'_c\right\|_{\mathrm{F}} + \left\|\hat{\boldsymbol{\sigma}}'_c \hat{\boldsymbol{n}}_c^{\mathrm{T}} \boldsymbol{x}_c\right\| + \|\boldsymbol{m}_c\|_1\right) \\ &= \psi_{c\omega}^* \cdot s_{c\omega}, \end{aligned} \tag{36}$$

where $c = h, v$. Define $\psi_{c\omega}^* \triangleq \max\left\{\|\boldsymbol{n}_c\|_{\mathrm{F}}, \|\boldsymbol{m}_c\|, \|\boldsymbol{m}_c\|_1\right\}$, $s_{c\omega} \triangleq \left\|\boldsymbol{x}_c \hat{\boldsymbol{m}}_c^{\mathrm{T}} \hat{\sigma}'_c\right\|_{\mathrm{F}} + \left\|\hat{\sigma}'_c \hat{\boldsymbol{n}}_c^{\mathrm{T}} \boldsymbol{x}_c\right\| + \|\boldsymbol{m}_c\|_1$. Considering that $\psi_{c\omega}^*$ is an unknown coefficient, while $s_{c\omega}$ is a known function. Bringing equation (35) into the Taylor expansion of equation (32), we get

$$\begin{aligned} \boldsymbol{\theta}_1 \circ \dot{\boldsymbol{\alpha}}_2 = -\boldsymbol{k}_2 \circ \boldsymbol{\alpha}_2 - \Phi^{\mathrm{T}} \circ \tilde{\Theta} + \tilde{\boldsymbol{M}}^{\mathrm{T}} \circ \left(\hat{\boldsymbol{\sigma}} - \hat{\boldsymbol{\sigma}}' \circ \hat{\boldsymbol{N}}^{\mathrm{T}} \circ \boldsymbol{X}\right) \\ + \hat{\boldsymbol{M}}^{\mathrm{T}} \circ \hat{\boldsymbol{\sigma}}' \circ \tilde{\boldsymbol{N}}^{\mathrm{T}} \circ \boldsymbol{X} + \boldsymbol{\omega} + \boldsymbol{\varepsilon}_{\mathrm{approx}} + \boldsymbol{i}_{\mathrm{s2}}. \end{aligned} \tag{37}$$

Step 4: In this step, the development of a nonlinear robust feedback component aims to mitigate the estimation inaccuracies in both parameter approximation and model uncertainty, encompassing errors $\tilde{\Theta}$ and $\boldsymbol{\varepsilon}_{\mathrm{approx}}$, thereby enhancing the overall system performance.

Thus, the system will remain stable and the control performance of the system will be improved. Consequently, this results in devising $\boldsymbol{i}_{\mathrm{s2}}$ to ensure a stable system that complies with the specified settling conditions outlined in the analysis. That is

$$\begin{aligned} \alpha_{c2}\left(i_{cs2} + \omega_c + \varepsilon_{c\mathrm{approx}}\right) &\leq \varepsilon_{cs} \\ \alpha_{c2} i_{cs2} &\leq 0, \end{aligned} \tag{38}$$

where $c = h, v$, ε_{hs} and ε_{vs} are arbitrarily small positive controller parameters that describe the robust capability of the controller. Introducing $h_{cs} \geq \psi_{c\omega}^* \cdot s_{c\omega} + |\varepsilon_{cN}|$ to represent an upper bound on all errors, then there are

$$i_{cs2} = -k_{cs} \cdot \alpha_{c2} - \frac{h_{cs}^2}{4\varepsilon_{cs}} \cdot \alpha_{c2}. \tag{39}$$

In many cases the h_{cs} in the controller cannot be obtained accurately. In order that h_{cs} can achieve accurate parameter adaption, it is necessary to redesign i_{cs2}. The redesign equation is as

$$\boldsymbol{i}_{\mathrm{s2}} = \hat{\boldsymbol{h}}_s \circ \mathrm{sgn}\left(\boldsymbol{\alpha}_2\right), \tag{40}$$

where $\boldsymbol{h}_s = [h_{hS}, h_{vS}]$, $\hat{\boldsymbol{h}}_s = \left[\hat{h}_{hS}, \hat{h}_{vS}\right]$ denotes the estimated value of $\boldsymbol{h}_s$.

At this juncture, the design and implementation of an adaptive robust controller integrated with RBF neural network compensation have been successfully completed. This proposed controller showcases sustained final boundedness, enabling it to maintain the tracking error within a predefined range over a limited duration. A detailed stability analysis that supports the effectiveness of the controller is provided in APPENDIX. The series of analyses indicated that the proposed controller can be employed for TGCS.

In the upcoming sections, a two-pronged verification approach will be employed. Firstly, a software-based verification model will be established to assess the feasibility of the control algorithm in a simulated environment. Secondly, a semi-physical model will be constructed to demonstrate the superiority of the controller algorithm when applied to real-world scenarios. These models will further reinforce the practicality, efficiency, and robustness of the adaptive controller with RBF neural network compensation. Detailed explanations of the modeling techniques employed, as well as insights into their respective results and implications for the overall system performance, will be discussed in subsequent sections.

IV. CO-SIMULATION VERIFICATION

A. OVERALL PROGRAM

In this part of the study, various road class models are created using the harmonic superposition method. The dynamic model of the TGCS is developed employing RecurDyn, with the controller implementation achieved through writing S-Functions in MATLAB/Simulink. A real-time co-simulation between the control algorithm and the multibody dynamics model is facilitated using an interface module. Subsequently, RecurDyn's measurement module gathers motion posture information for both the turret and the barrel, which is then transferred to MATLAB/Simulink. Within the MATLAB/Simulink environment, the control algorithm computes the theoretical control moments for the turret and barrel. These values are then conveyed back to the RecurDyn environment as rotational axial forces, enabling a seamless co-simulation process. Fig. 7 illustrates the co-simulation principle of the TGCS employed in this particular section of the study.

B. ESTABLISHMENT OF THE MOVING TANK

1) ROAD ROUGHNESS

The primary determinant of fluctuations of the tank gun is the stimulation induced by the road conditions. Hence, the initial step in constructing a comprehensive model of a tank involves establishing a model of unevenness in the pavement. As the tank moves, the stimulation originating from the road is transmitted to the tracks, suspension system, hull, turret, and barrel. Consequently, this leads to the application of vibrational forces at the muzzle, thereby influencing the angle of the projectile as it departs from the barrel during the firing process, thereby compromising the overall accuracy of firing.

The indicator representing the roughness of the road is a smooth Gaussian process that takes into account the actual statistical properties of the pavement, typically depicted by the power spectral density in the frequency domain. By employing a classification system based on profiles of road, one can ascertain the power spectral density for different

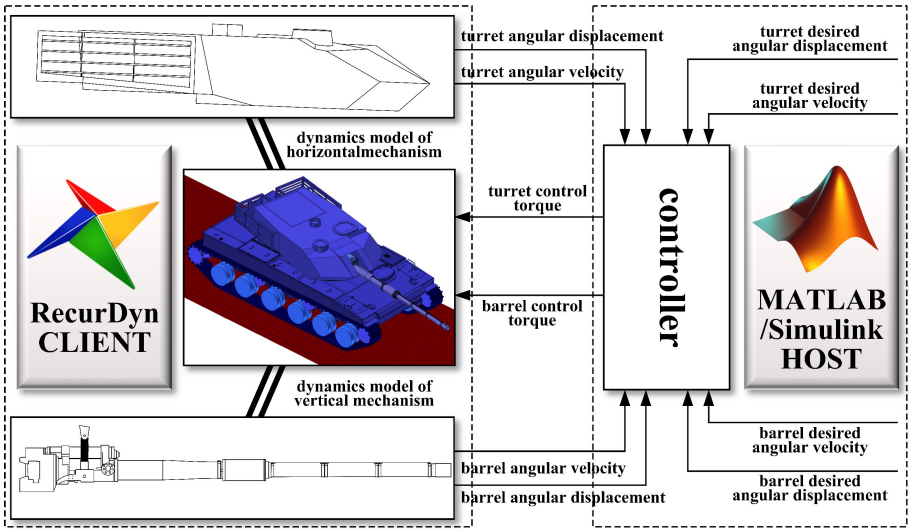

FIGURE 7. Schematic diagram of co-simulation.

road roughness. The expression for this is as

$$G_q(n) = G_q(n_0)\left(\frac{n}{n_0}\right)^{-w}, \tag{41}$$

where $n = 1/\lambda$ represents the spatial frequency, denoting the number of wavelengths contained in each meter of road length, with λ signifying the wavelength; n_0 represents the reference spatial frequency; $G_q(n_0)$ stands for the coefficient of road roughness, indicating the power spectral density value of the road at the reference spatial frequency n_0; and w is the frequency exponent, determining the frequency structure of the road power spectral density. Based on the power density spectrum of the road, the roughness of the road can be categorized into eight levels: A to H.

The pavement spatial frequency is divided into N intervals. Approximating the power spectral density value $G_q(f_i)$ corresponding to the central frequency f_i $(i = 1, 2, \ldots, N)$ of the i-th interval n_i instead of the whole interval value, the stochastic process of pavement unevenness can be expressed as

$$q(x) = \sum_{i=1}^{N}\left\{\sqrt{2}A_i \cdot \sin\left[2\pi\left(n_i x + \alpha_i\right)\right]\right\}, \tag{42}$$

where the x-direction is the direction along the road, α_i represents a random number that is uniformly distributed within a certain interval $[0, 1]$. A_i represents the harmonic vibration amplitude corresponding to the center frequency f_i, expressed as

$$A_i = \sqrt{G_q(f_i) \cdot \Delta n}. \tag{43}$$

Moreover, during actual driving, the excitations from the road are not identical on both the tank's left and right tracks. The coherence of the road excitation on both sides of the tracks can be represented as

$$\gamma(n) = \begin{cases} e^{-\rho n d_v} & n \in (n_1, n_2) \\ 0 & n \notin (n_1, n_2), \end{cases} \tag{44}$$

where d_v is the track gauge, p is an empirical coefficient, and n_1, n_2 are the upper and lower limits of the road spatial frequency. The random phase angle α_{Ri} of the left and right tracks under road stimulation is the primary factor causing the differences in excitation. Based on equation (44), the expression for α_{Ri} can be obtained as

$$\alpha_{Ri} = \frac{e^{-2\pi d_v n^{1.5}}\alpha_i + \sqrt{1 - e^{-2\pi x n^{1.5}}}\alpha_n}{\sqrt{1 - e^{-2\pi d_v n^{1.5}}} + e^{-2\pi d_v n^{1.5}}}. \tag{45}$$

where α_n is the newly generated random number in $[0, 1]$.

By combining Equation (42) and Equation (45), the stochastic process of 3D pavement unevenness can be expressed as

$$q(x, y) = \sum_{i=1}^{N}\left\{\sqrt{2}A_i \cdot \sin\left[2\pi\left(n_i x + \alpha_y\right)\right]\right\} \tag{46}$$

and

$$\alpha_y = \frac{e^{-2\pi y n^{1.5}}\alpha_i + \sqrt{1 - e^{-2\pi y n^{1.5}}}\alpha_n}{\sqrt{1 - e^{-2\pi y n^{1.5}}} + e^{-2\pi y n^{1.5}}}, \tag{47}$$

where the y-direction represents the direction perpendicular to the road, and a represents the random phase of the road unevenness excitation in the y-direction.

In this study, the pavement is reconstructed using the harmonic superposition method, and a program is developed to generate random pavement roughness based on mathematical tools. Pavement model with dimensions of 300m in length and 10m in width is established. Software-readable pavement files are generated using the joint seam method. The pavement model of class F is shown in Fig. 8. This road

roughness class is generally the maximum roughness that tanks are allowed to shoot at during high speed travel in the actual battlefield.

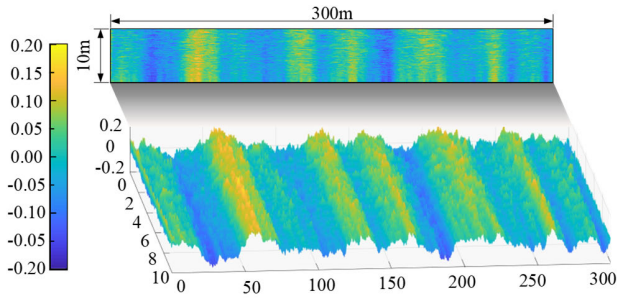

FIGURE 8. Pavement model of class F.

2) MULTIBODY DYNAMICS MODEL OF TANK

The multibody dynamics model of the tank considered in this study consists primarily of the chassis part and the fire system part, ignoring the power part and the transmission part. The chassis part mainly includes the hull, suspensions, idle wheels, towing wheels, driving wheels, loading wheels and tracks, etc. The fire system part mainly includes the barrel, gun breech, cradle, electric cylinder, anti-recoil devices and turret, etc. Fig. 9 shows the entirely all-electric tank topology. The components are connected by standard hinges except for the consideration of contacts for barrel and bushings and contacts for trunnion bearings. The forces of the recoil mechanism and recuperator mechanism are fitted by interpolation functions and loaded directly at the appropriate positions, respectively. Meanwhile, the modeling completely describes the external uncertainty disturbances and the uncertainties in TGCS, and the software RecurDyn is used to model the multibody dynamics model of an actual type of tank, which is our co-simulation object communicated with MATLAB/Simulink, as shown in Fig. 10.

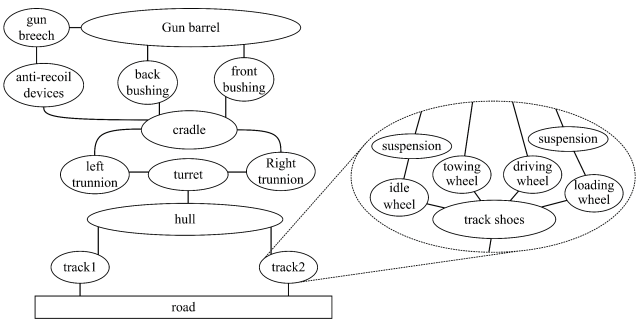

FIGURE 9. Topological relationship of connection modes of main assemblies of tank system.

C. CO-SIMULATION RESULT

Keep the tank at 40km/h on class F roads. According to the 8 road roughness classes proposed by ISO, the base parameters of road roughness are set as $n_0 = 0.1\text{m}^{-1}$, $w = 2$ and

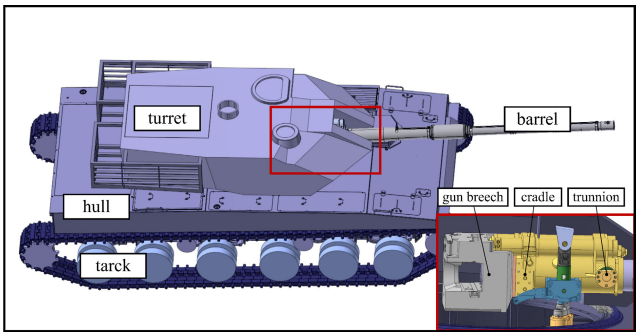

FIGURE 10. Multibody dynamics model of the moving tank built in RecurDyn.

$G_q(n_0) = 16384 \times 10^{-6}\text{m}^3$. The rest of the parameters related to the co-simulation are shown in Table 2.

In addition, PID controller and ARC controller are picked for comparison to prove and verify the effectiveness of the proposed controller. The introduction of the controller and the specific parameters are shown below.

1) ARCNN. The ARC controller based on RBFNN compensation is proposed in this paper. In the horizontal direction, the control gains $k_1 = 1500$ and $k_2 = 840$ are chosen. In the horizontal direction, the control gains $k_1 = 2300$ and $k_2 = 1250$ are chosen. The adaptive speed matrix is set to $\mathbf{\Gamma} = \text{diag}\{0.005, 0.005, 0.005\}$. The node number of the hidden layer is given as 8. The initial value of the NN is given as 0.1.
2) ARC. The conventional adaptive robust control, using disturbance observer for compensated control, without using RBFNN compensation. Its parameters are the same as those of the ARCNN described above.
3) PID. The most widely used control method in modern TGCS is tuned by three main parameters K_p, K_i and K_d. In the horizontal direction, choose its control parameters $K_p = 1200$, $K_i = 60$ and $K_d = 15$. In the vertical direction, choose its control parameters $K_p = 1400$, $K_i = 35$ and $K_d = 5$.

Assume the following conditions, our tank is moving at 40km/h on a class F road. The enemy tank is moving around our tank at constant speed. Our tank finds the target at 2s and the turret and barrel start to move and point at the enemy target. Fig. 11(a) and (b) show the angular real-time positions of the tank muzzle. The desired angle is the angle of the enemy target returned by the sighting system. In the first 2s, the tank maintains a 0-degree shooting angle but still has slight fluctuations due to various reasons such as vehicle speed and road roughness. At the 2s, the tank detects the target and the error between the target angle and the actual angle starts to decrease gradually under the action of the controller. The proposed controller can track the enemy target faster, more concentrated and more stable compared with other controllers. The ARC controller, although showing a slightly faster tracking speed than the PID controller in the

TABLE 2. Main parameters in co-simulation experiment.

	Parameter	Symbol	Value	Unit
Dynamics-related	Gravitational acceleration	g	9.80	m/s^2
	Mass of horizontal direction	m_h	5200.00	kg
	Mass of vertical direction	m_v	2048.70	kg
	Inertia of horizontal direction	J_h	6900.00	$kg \cdot m^2$
	Inertia of vertical direction	J_v	3448.00	$kg \cdot m^2$
	Estimated transmission ratio of horizontal direction	n_h	204	-
	Estimated transmission ratio of vertical direction	n_v	12	-
Motor-related	Hysteresis coefficient of the motor in the horizontal direction	B_h	1.2e-3	$N \cdot m \cdot s/rad$
	Hysteresis coefficient of the motor in the vertical direction	B_v	1.5e-3	$N \cdot m \cdot s/rad$
	Torque coefficient of the motor in the horizontal direction	K_{hT}	1.89	$N \cdot m/A$
	Torque coefficient of the motor in the vertical direction	K_{vT}	1.54	$N \cdot m/A$

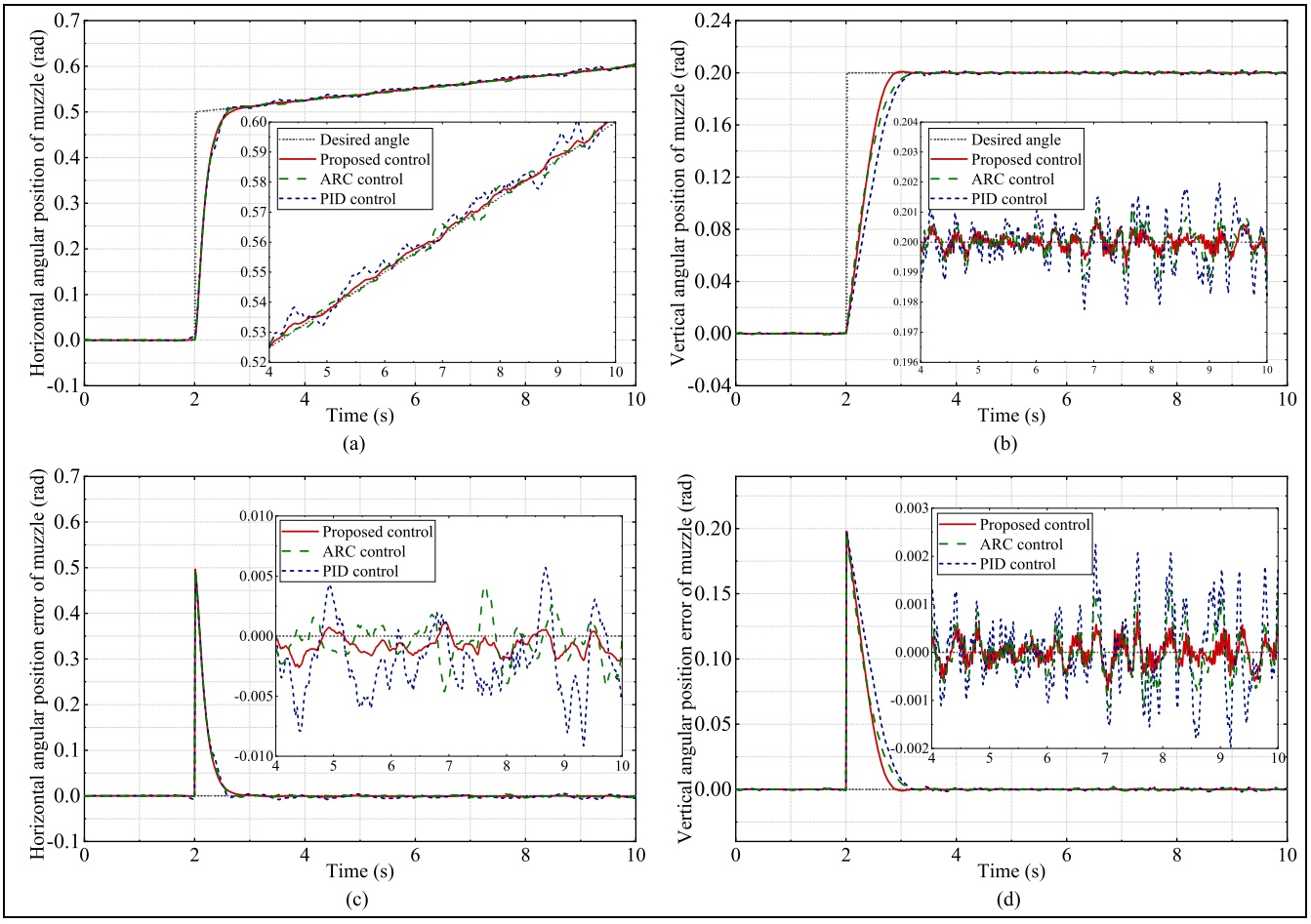

FIGURE 11. Real time muzzle angular position and error in the co-simulation experiment: (a) horizontal angular position of muzzle, (b) vertical angular position of muzzle, (c) horizontal angular position error of muzzle, and (d) vertical angular position error of muzzle.

bidirectional direction, is still a bit worse than the proposed controller. In particular, after 4s, both the ARC controller and the PID controller perform much worse than the proposed controller in terms of tracking accuracy and root-mean-square of error. The proposed controller exhibits smaller magnitudes. This is thanks to the advantage of RBFNN estimation.

TABLE 3. Comparison of stabilization effects.

The projects involved	Horizontal rotation angle			Vertical rotation angle		
	PID	ARC	Proposed	PID	ARC	Proposed
Tracking accuracy (mrad)	02.1664	01.5153	00.3704	04.3189	03.1485	01.6450
Extreme value of error (mrad)	08.2625	06.1852	01.7478	21.7219	16.9375	09.1014
Root-mean-square of error (mrad)	00.8461	00.7835	00.3593	01.6496	01.3582	01.0177

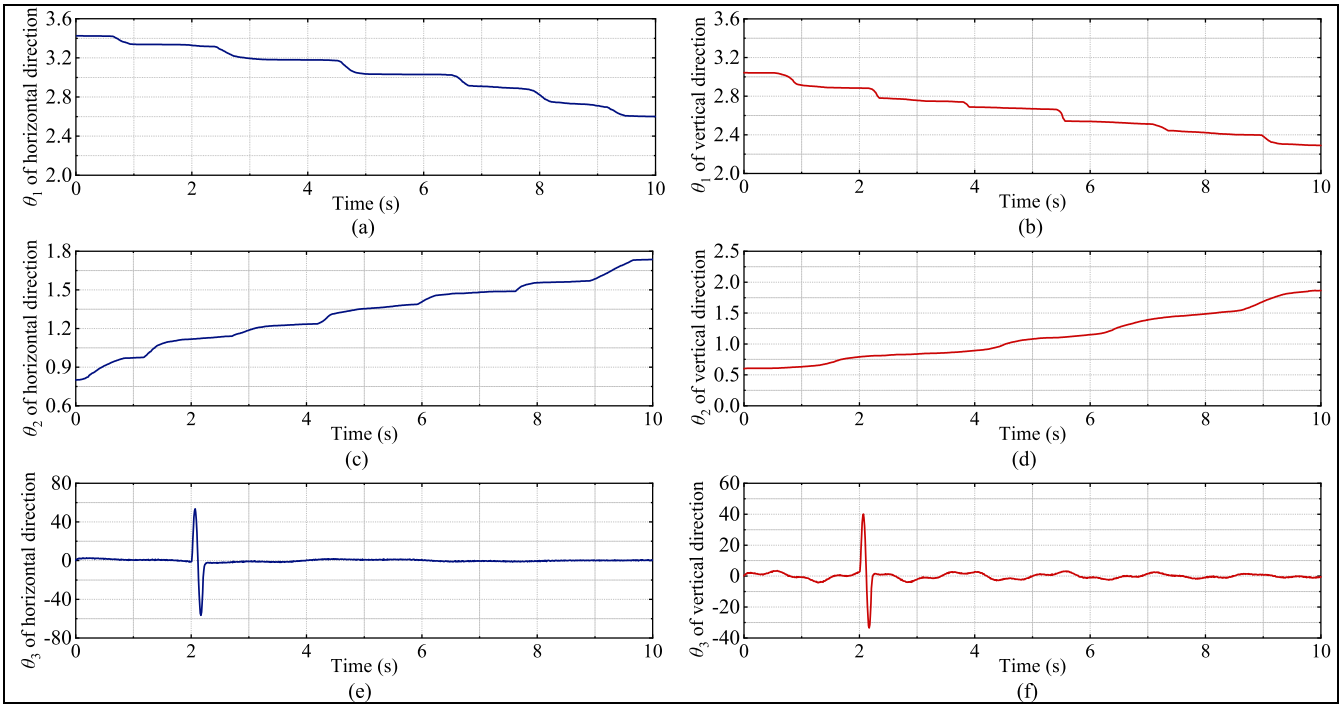

FIGURE 12. Adaptive parameters of the control in horizontal and vertical direction: (a) θ_1 of horizontal direction, (b) θ_1 of vertical direction, (c) θ_2 of horizontal direction, (d) θ_2 of vertical direction, (e) θ_3 of horizontal direction and (f) θ_3 of vertical direction.

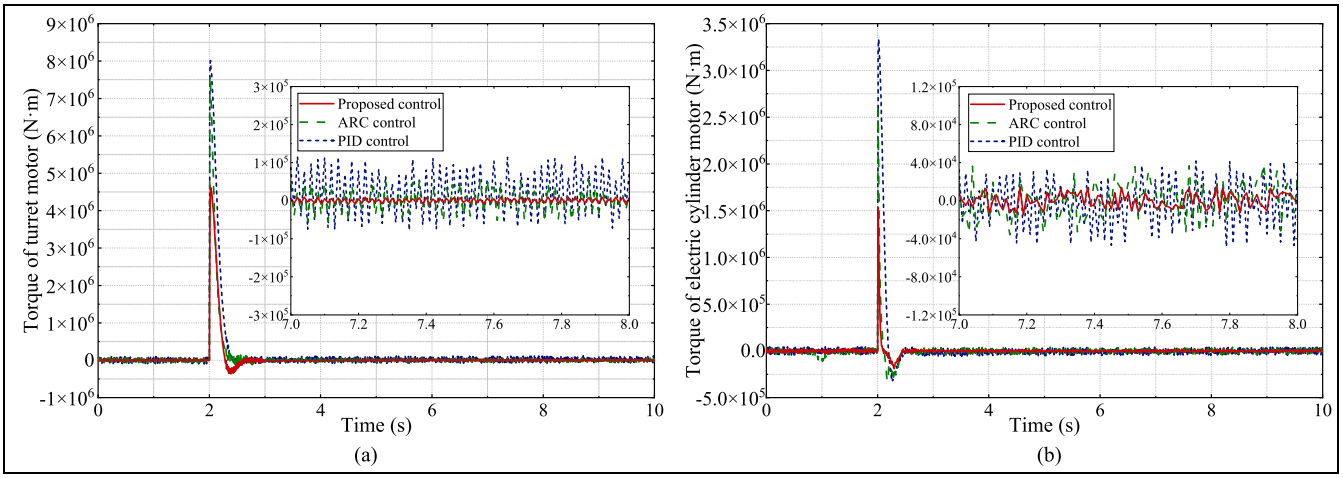

FIGURE 13. Comparison of the torque input: (a) comparison of the turret motor, and (b) comparison of the electric cylinder motor.

Fig. 11(c) and (d) show the angular real-time position errors of the muzzle in the bidirectional direction. The error feedback can be visualized more precisely to show the performance of the controller. Also, the muzzle control information for 6-10 seconds is summarized in Table 3.

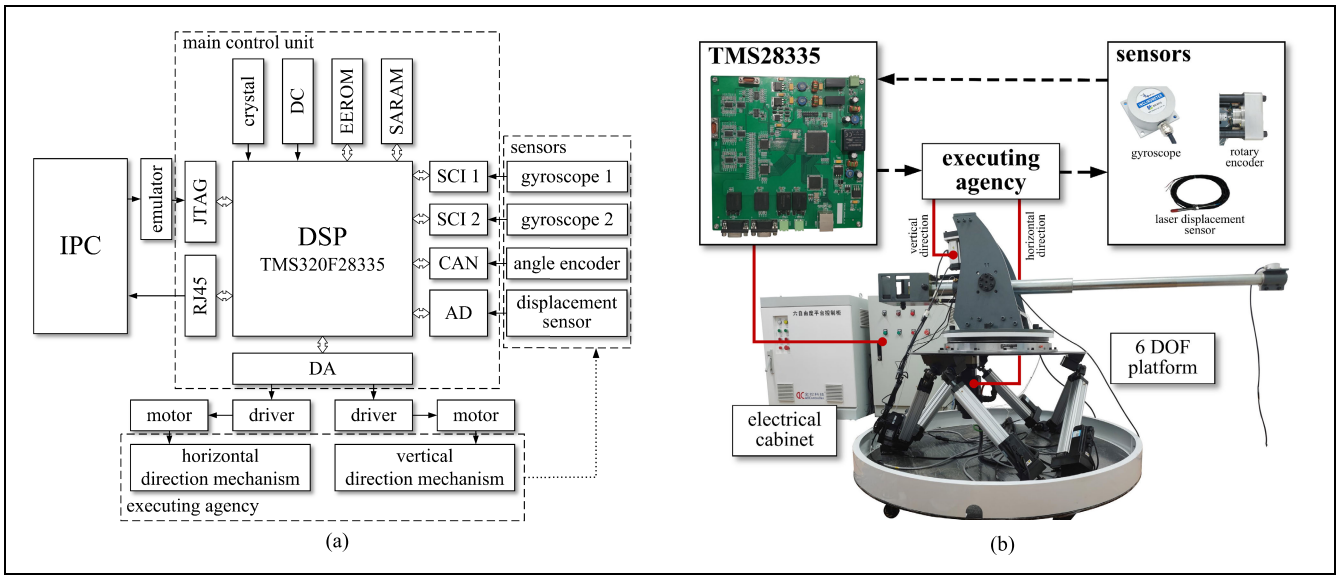

FIGURE 14. Semi-physical simulation platform experiment: (a) system composition and (b) interaction principle.

TABLE 4. Main parameters in semi-physical simulation platform.

	Parameter	Symbol	Value	Unit
Dynamics-related	Gravitational acceleration	g	9.80	m/s^2
	Mass of horizontal direction	m_h	173.15	kg
	Mass of vertical direction	m_v	71.01	kg
	Inertia of horizontal direction	J_h	27.21	$kg \cdot m^2$
	Inertia of vertical direction	J_v	17.03	$kg \cdot m^2$
	Estimated transmission ratio of horizontal direction	n_h	200	-
	Estimated transmission ratio of vertical direction	n_v	6	-
Motor-related	Hysteresis coefficient of the motor in the horizontal direction	B_h	7.2e-4	$N \cdot m \cdot s/rad$
	Hysteresis coefficient of the motor in the vertical direction	B_v	5.3e-4	$N \cdot m \cdot s/rad$
	Torque coefficient of the motor in the horizontal direction	K_{hT}	0.91	$N \cdot m/A$
	Torque coefficient of the motor in the vertical direction	K_{vT}	0.05	$N \cdot m/A$

Based on the results presented in Table 3, it is evident that the proposed controller exhibits better stability and accuracy. The proposed controller is better able to satisfy the needs of the battlefield compared to the other two controllers. The adaptive parameters of the designed controller are shown in Fig. 12.

Obviously, the ARC is superior to the PID because the ARC model-based control strategy compensates well for the known information in the model, and the robustness is enhanced by the adaptive technique and the non-linear robustness term. Furthermore, it can be found that the proposed ARCNN controller outperforms the ARC and PID controllers. The proposed controller is effective because the adaptive control is used to estimate the unknown parameters of the system well. The nonlinear robustness term enhances the stability performance of the system. The neural network approximates and compensates feedforward well for the uncertain nonlinear and unmodelled dynamics. As a result, the proposed controller performs optimally in terms of control performance. All co-simulation results verify the effectiveness of the proposed controller in this paper.

The real-time output torque of the motor controlling the horizontal motion of the turret, and the motor of the electric cylinder controlling the vertical motion of the barrel are shown in Fig. 13. The comparison of the output torque can directly reflect the control cost of the controller. At the moment of enemy detection, the proposed controller consumes fewer instantaneous control torque. The ARC controller has a slightly smaller transient torque when the enemy tank is detected compared to the PID controller, but the

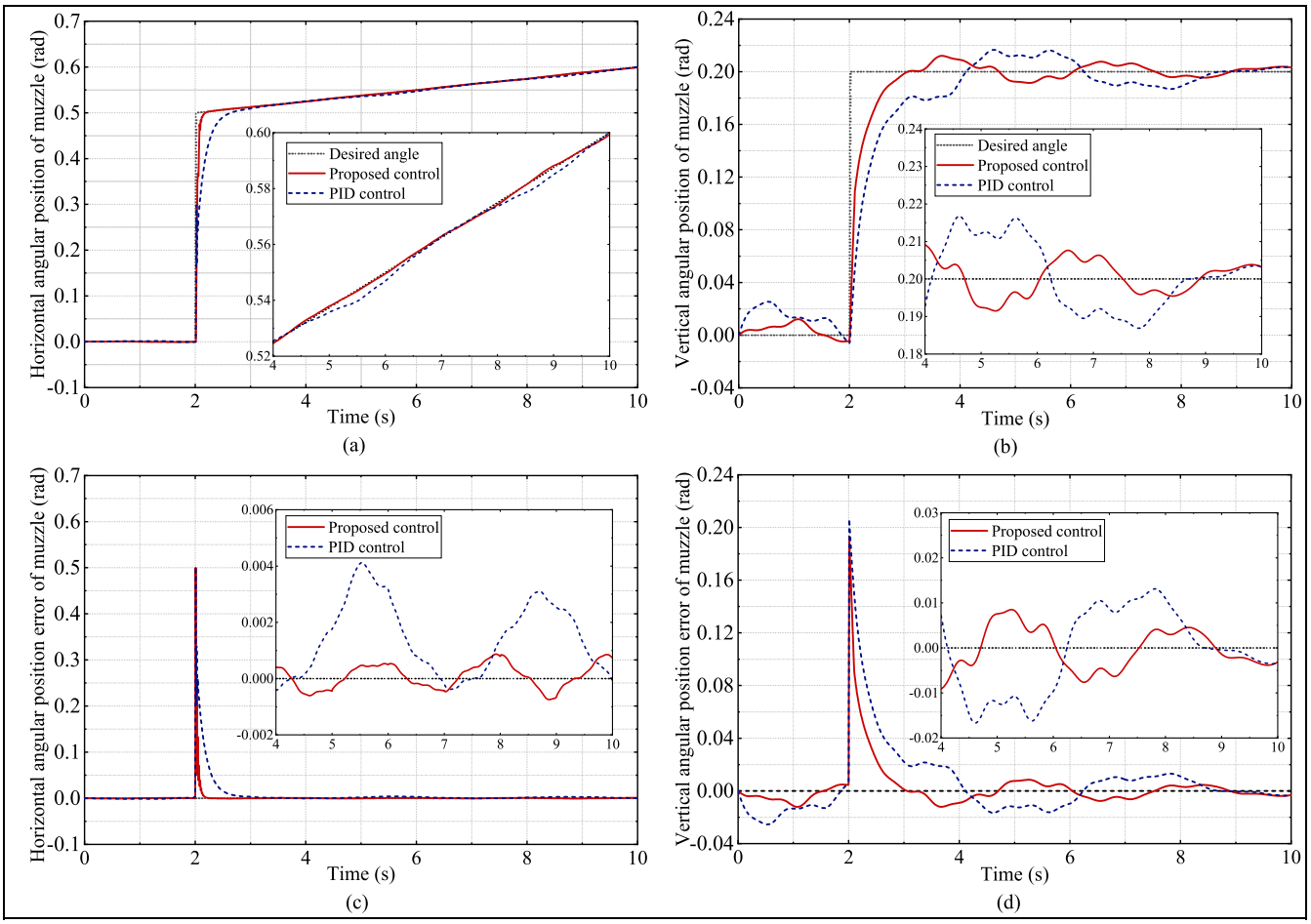

FIGURE 15. Real time muzzle angular position and error in the semi-physical platform experiment: (a) horizontal angular position of muzzle, (b) vertical angular position of muzzle, (c) horizontal angular position error of muzzle, and (d) vertical angular position error of muzzle.

performance is not much improved after stabilization. And after reaching control stability, the fluctuation amplitude of the torque is evidently smaller than that of the other two controllers, and the fluctuation period is slightly larger than that of the other two controllers. This means that the proposed controller not only has a smaller control cost, but also has an essential significance in improving the lifetime of the tank motor.

V. EXPERIMENT VERIFICATION

A. PLATFORM COMPOSITION

The semi-physical simulation platform of TGCS is driven by PMSM in both vertical and horizontal directions. The main control unit uses the same high-performance DSP chip as the real tank gun, which is chosen as TMS320F28335. In order to guarantee the timing of the control, the same CPU is used in bidirectional direction. The IPC performs program burn-in of TMS320F28335 via JTAG. The programs involved include the main program, reset program, interrupt program and sensor acquisition program, etc. The RJ45 port is used to facilitate the debugging of control parameters. At any moment, an analog signal is sent to the motor driver through the DA port, the motor will move and thus the semi-physical platform will work. Simultaneously, sensors will collect the motion data and feed the data back to TMS320F28335 through SCI, CAN and AD ports. The controller will calculate the analog value for the next moment based on the data collected back. The overall scheme is shown in Fig. 14. The overall system composition is shown in Fig. 14(a), and the system interaction principle is shown in Fig. 14(b).

The road excitation data in the semi-physical simulation platform is derived from the data of measuring real moving tank, which is scaled down equally for the scale of the experimental platform. The rest experimental platform parameters are presented in Table 4.

B. EXPERIMENT RESULT

Firstly, the experiment was done on the experimental platform with the same control commands, the same vehicle speed, and the same road roughness as the co-simulation. Let the tank with 40km/h speed detect the enemy target and track and point. This condition is typically the extreme bad shooting condition of the tank in the actual battlefield. The experiment data is shown in Fig. 15. It can be observed that the

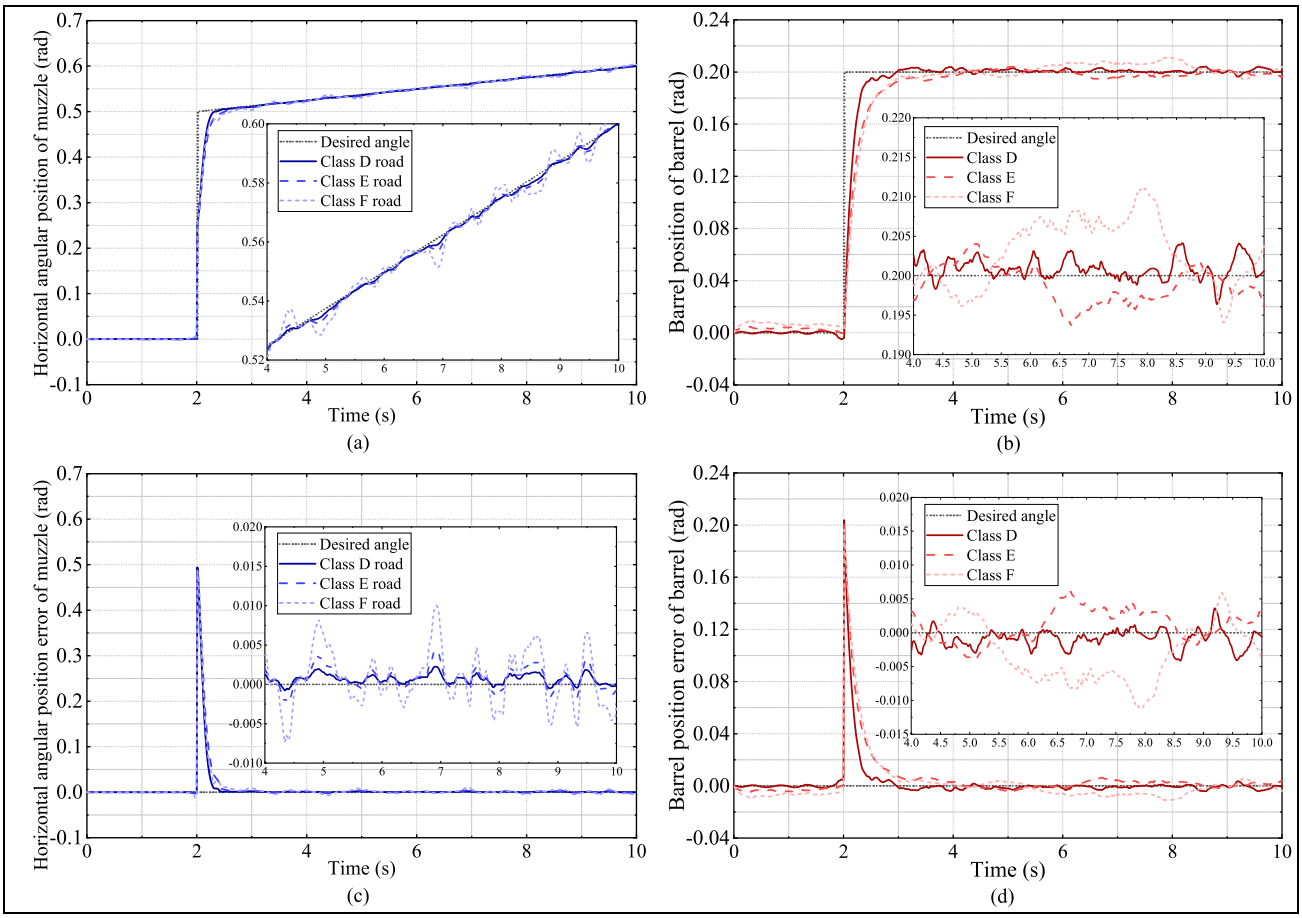

FIGURE 16. Real time muzzle angular position and error for different road roughness with proposed controller: (a) horizontal angular position of muzzle, (b) vertical angular position of muzzle, (c) horizontal angular position error of muzzle, and (d) vertical angular position error of muzzle.

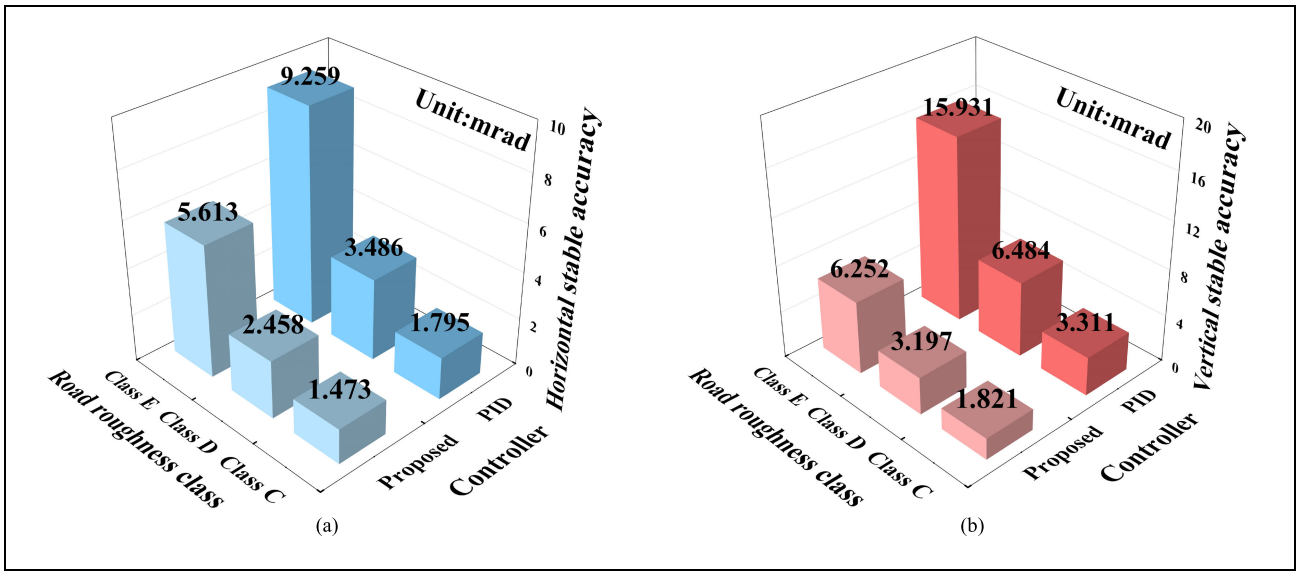

FIGURE 17. Stability accuracy of two controllers at different road roughness class: (a) horizontal stability accuracy and (b) vertical stability accuracy.

angular displacement of the muzzle in the vertical direction is more sensitive to the disturbance than in the horizontal direction, which is compounded by the experiment results of the actual tank. At the same time, the controller can still achieve bidirectional control of the tank under extreme conditions, and it performs significantly better than PID control.

Faster control speed and smaller tracking accuracy are exhibited. The overall experimental results of the experimental platform match the co-simulation results.

Additionally, different levels of road roughness result in varying control errors for the tank. To assess the robustness of the proposed controller, experimental platform simulations were conducted on three distinct road surface grades under identical control commands. The robustness evaluation of the controller can be achieved by introducing progressively worse road roughness classes. A co-experiment validation comparing the proposed controller and the PID controller was performed, utilizing vibration data from various road roughness conditions. The performance of the proposed controller is illustrated in Fig. 16. As the road conditions become more challenging, the controller's effectiveness gradually declines, yet it maintains a high-quality control response. As the road class worsens, both the magnitude and the period of the muzzle angle variation increase. In order to quantify the effectiveness of the controller, the absolute average error within a finite period of time—after achieving control stability—is commonly employed in artillery firing research to characterize tank gun stability accuracy. The expression is

$$\mu_\theta = \frac{1}{n}\sum_{i=1}^{n}|\theta_i|, \tag{48}$$

where n is the total number of sampling points in a period of time after reaching stability and θ_i is the angular position error at $n = i$. The results of the above experiments with different road roughness are calculated and analyzed ranging from 4 to 6s. The stable performance of both controllers under different conditions can be obtained. Their comparison pairs with PID controllers are shown in Fig. 17.

As the road roughness increases, the control error correspondingly grows larger. It can be observed that the performance of the PID controller degrades in comparison to the proposed controller, in both horizontal and vertical directions.

VI. CONCLUSION

In this study, we develop an electromechanical coupling model for the moving tank and construct an adaptive robust controller based on torque control with RBFNN compensation tailored for the TGCS. With regard to the proposed controller, adaptive techniques solve the problem of parameter uncertainties in the system. RBFNN is used to approximate the uncertainty nonlinearities and compensated via feedforward. Robust techniques suppress residual uncertainties in the system. This approach effectively addresses the motion target tracking problem in the moving tank's TGCS, allowing the muzzle to be precisely adjusted from the initial position to the target position and kept stable in the bidirectional direction. To validate the controller, we not only propose a multibody dynamics model with road roughness considerations for co-simulation verification, but also present a semi-physical simulation scheme for TGCS. The validation results consistently demonstrate the proposed controller's exceptional robustness against strong external disturbances. Outstanding performance has been achieved in dealing with strong parameter uncertainties and uncertain nonlinearities. This research contributes a novel control method for managing complex mechanical systems, with potential for further extension to other control methodologies and nonlinear models.

APPENDIX
STABILITY ANALYSIS

Based on the previously designed controller, we can obtain the control rate $\boldsymbol{i}_q$ of PMSM as

$$\begin{aligned}\boldsymbol{i}_q &= \hat{\boldsymbol{\theta}}_1 \circ \dot{\boldsymbol{\alpha}}_2 + \hat{\boldsymbol{\theta}}_2 \circ x_2 + \hat{\boldsymbol{\theta}}_3 + \hat{\boldsymbol{\tau}}_{d1} - \boldsymbol{k}_2 \circ \boldsymbol{\alpha}_2 + \boldsymbol{i}_{s2} \\ &= -\Phi^{\mathrm{T}} \circ \hat{\Theta} + \hat{\boldsymbol{\tau}}_{d1} - \boldsymbol{k}_2 \circ \boldsymbol{\alpha}_2 + \boldsymbol{i}_{s2}. \end{aligned} \tag{A.1}$$

It follows the following adaptive law

$$\begin{aligned}\dot{\hat{\Theta}} &= \boldsymbol{\Gamma} \circ \Phi \circ \boldsymbol{\alpha}_2 \\ \dot{\hat{\boldsymbol{M}}} &= -\boldsymbol{G} \circ \boldsymbol{\alpha}_2 \circ \left(\hat{\sigma} - \hat{\sigma}' \circ \hat{\boldsymbol{N}}^{\mathrm{T}} \circ \boldsymbol{X}\right) \\ \dot{\hat{\boldsymbol{N}}} &= -\boldsymbol{F} \circ \boldsymbol{X} \circ \hat{\boldsymbol{M}}^{\mathrm{T}} \circ \hat{\sigma}' \circ \boldsymbol{\alpha}_2, \end{aligned} \tag{A.2}$$

where $\boldsymbol{\Gamma}$ is the adaptive velocity matrix and $\boldsymbol{G}, \boldsymbol{F} > 0$ are positive definite symmetric matrices.

Define the Lyapunov function v as

$$\begin{aligned}V = &\frac{1}{2}\boldsymbol{\theta}_1 \circ \boldsymbol{\alpha}_2 \circ \boldsymbol{\alpha}_2 + \frac{1}{2}\tilde{\Theta}^{\mathrm{T}} \circ \boldsymbol{\Gamma}^{-1} \circ \tilde{\Theta} \\ &+ \frac{1}{2}\tilde{\boldsymbol{M}}^{\mathrm{T}} \circ \boldsymbol{G}^{-1} \circ \tilde{\boldsymbol{M}} + \frac{1}{2}\tilde{\boldsymbol{N}}^{\mathrm{T}} \circ \boldsymbol{F}^{-1} \circ \tilde{\boldsymbol{N}}. \end{aligned} \tag{A.3}$$

Its derivative with respect to time is

$$\begin{aligned}\dot{V} = &\boldsymbol{\theta}_1 \circ \dot{\boldsymbol{\alpha}}_2 \circ \boldsymbol{\alpha}_2 + \tilde{\Theta}^{\mathrm{T}} \circ \boldsymbol{\Gamma}^{-1} \circ \dot{\tilde{\Theta}} \\ &+ \tilde{\boldsymbol{M}}^{\mathrm{T}} \circ \boldsymbol{G}^{-1} \circ \dot{\tilde{\boldsymbol{M}}} + \tilde{\boldsymbol{N}}^{\mathrm{T}} \circ \boldsymbol{F}^{-1} \circ \dot{\tilde{\boldsymbol{N}}} \end{aligned} \tag{A.4}$$

Since Θ, $\boldsymbol{M}$ and $\boldsymbol{N}$ are time-invariant or slowly changing variables, we approximate that $\dot{\hat{\Theta}} = \dot{\tilde{\Theta}}, \dot{\hat{\boldsymbol{M}}} = \dot{\tilde{\boldsymbol{M}}}$ and $\dot{\hat{\boldsymbol{N}}} = \dot{\tilde{\boldsymbol{N}}}$. Bringing equations (37) and (A.2) into equation (A.4), we get

$$\begin{aligned}\dot{V} &= \boldsymbol{\theta}_1 \circ \dot{\boldsymbol{\alpha}}_2 \circ \boldsymbol{\alpha}_2 + \tilde{\Theta}^{\mathrm{T}} \circ \boldsymbol{\Gamma}^{-1} \circ \dot{\tilde{\Theta}} + \tilde{\boldsymbol{M}}^{\mathrm{T}} \circ \boldsymbol{G}^{-1} \circ \dot{\tilde{\boldsymbol{M}}} \\ &\quad + \tilde{\boldsymbol{N}}^{\mathrm{T}} \circ \boldsymbol{F}^{-1} \circ \dot{\tilde{\boldsymbol{N}}} \\ &= -\boldsymbol{k}_2 \circ \boldsymbol{\alpha}_2^2 + \boldsymbol{\Gamma}^{-1} \circ \tilde{\Theta}^{\mathrm{T}} \circ \left(\dot{\tilde{\Theta}} - \boldsymbol{\Gamma} \circ \Phi \circ \boldsymbol{\alpha}_2\right) \\ &\quad + \tilde{\boldsymbol{M}}^{\mathrm{T}} \circ \left(\hat{\sigma} - \hat{\sigma}' \circ \hat{\boldsymbol{N}}^{\mathrm{T}} \circ \boldsymbol{X}\right) \circ \boldsymbol{\alpha}_2 \\ &\quad + \tilde{\boldsymbol{M}}^{\mathrm{T}} \circ \boldsymbol{G}^{-1} \circ \dot{\tilde{\boldsymbol{M}}} \\ &\quad + \tilde{\boldsymbol{N}}^{\mathrm{T}} \circ \boldsymbol{F}^{-1} \circ \dot{\tilde{\boldsymbol{N}}} \\ &\quad + \boldsymbol{\alpha}_2 \circ \left(\boldsymbol{\omega} + \boldsymbol{\varepsilon}_{\text{approx}} + \boldsymbol{i}_{s2}\right) \\ &= -\boldsymbol{k}_2 \circ \boldsymbol{\alpha}_2^2 + \boldsymbol{\alpha}_2 \circ \left(\boldsymbol{\omega} + \boldsymbol{\varepsilon}_{\text{approx}} + \boldsymbol{i}_{s2}\right) \\ &\leq -\boldsymbol{k}_2 \circ \boldsymbol{\alpha}_2^2 + \boldsymbol{\varepsilon}_s \\ &\leq \mathbf{0}. \end{aligned} \tag{A.5}$$

Through the above analysis, it can be found that the tracking error can achieve consistent ultimate boundedness by increasing the gain continuously.

ACKNOWLEDGMENT

The author Shusen Yuan sincerely thanks and appreciates his supervisor, Prof. Guolai Yang, whose suggestions and encouragement have given him much insight into these translation studies. It has been a great privilege and joy to study under his guidance and supervision. Furthermore, it is his honor to benefit from his personality and diligence, which he will treasure his entire life. His gratitude to him knows no bounds.

REFERENCES

[1] T. Dursun, F. Büyükcivelek, and Ç. Utlu, "A review on the gun barrel vibrations and control for a main battle tank," *Defence Technol.*, vol. 13, no. 5, pp. 353–359, Oct. 2017.

[2] H. Zheng, X. Rui, J. Zhang, S. Zhang, and J. Gu, "Improved modeling and active disturbance rejection control of tank gun control system," *Proc. Inst. Mech. Eng. I, J. Syst. Control Eng.*, vol. 236, no. 9, pp. 1649–1666, Jun. 2022.

[3] Z. Zhou, W. Wang, Y. Zhang, Q. Yan, and J. Cai, "Barrier adaptive iterative learning control for tank gun control systems under nonzero initial error condition," *IEEE Access*, vol. 10, pp. 8664–8672, 2022.

[4] Y. Chen and G. Yang, "Dynamic simulation of tank stabilizer based on adaptive control," *Proc. Inst. Mech. Eng. C, J. Mech. Eng. Sci.*, vol. 233, no. 9, pp. 3038–3049, May 2019.

[5] J. Shukla, "Dynamic analysis of gun control system of main battle tank," *Int. J. Heavy Veh. Syst.*, vol. 28, no. 2, pp. 158–183, Jun. 2021.

[6] Y. Chen, G. Yang, and Q. Sun, "Dynamic simulation on vibration control of marching tank gun based on adaptive robust control," *J. Low Freq. Noise, Vib. Act. Control*, vol. 39, no. 2, pp. 416–434, Jun. 2020.

[7] Q. Sun, X. Wang, G. Yang, Y.-H. Chen, and F. Ma, "Adaptive robust control for pointing tracking of marching turret-barrel systems: Coupling, nonlinearity and uncertainty," *IEEE Trans. Intell. Transp. Syst.*, vol. 23, no. 9, pp. 16397–16409, Sep. 2022.

[8] Q. Sun, X. Wang, G. Yang, Y.-H. Chen, and P. Duan, "Robust pointing control of marching tank gun with matched and mismatched uncertainty," *IEEE Trans. Cybern.*, vol. 52, no. 8, pp. 7303–7318, Aug. 2022.

[9] Q. Sun, G. Yang, X. Wang, and Y.-H. Chen, "Optimizing constraint obedience for mechanical systems: Robust control and non-cooperative game," *Mech. Syst. Signal Process.*, vol. 149, Feb. 2021, Art. no. 107207.

[10] Q. Gao, J. Chen, L. Wang, S. Xu, and Y. Hou, "Multiobjective optimization design of a fractional order PID controller for a gun control system," *Sci. World J.*, vol. 2013, May 2013, Art. no. 907256.

[11] A. B. Tatar, B. Taşar, and O. Yakut, "A shooting and control application of four-legged robots with a gun turret," *Arabian J. Sci. Eng.*, vol. 45, no. 7, pp. 5191–5206, Feb. 2020.

[12] J. Cai, R. Yu, Q. Yan, C. Mei, B. Wang, and L. Shen, "Event-triggered adaptive control for tank gun control systems," *IEEE Access*, vol. 7, pp. 17517–17523, 2019.

[13] Y. Ma, G. Yang, Q. Sun, X. Wang, and Q. Sun, "Adaptive robust control of moving-target tracking for marching tank based on constraint following," *Proc. Inst. Mech. Eng. D, J. Automobile Eng.*, vol. 236, no. 9, pp. 2087–2102, Aug. 2022.

[14] Y. Ma, G. Yang, Q. Sun, X. Wang, and Q. Sun, "Adaptive robust control for tank stability: A constraint-following approach," *Proc. Inst. Mech. Eng. I, J. Syst. Control Eng.*, vol. 235, no. 1, pp. 3–14, Jan. 2021.

[15] C. Li, G. Yang, X. Wang, Y. Ma, L. Wang, and Q. Sun, "Adaptive robust target tracking control of marching tank under high-speed maneuvering condition," *J. Mech. Sci. Technol.*, vol. 36, no. 6, pp. 2787–2798, Jun. 2022.

[16] C. Li, X. Wang, Q. Sun, and G. Yang, "Adaptive robust control of muzzle vibration for marching tank based on disturbance observer," in *Proc. Int. Conf. Adv. Robot. Mechatronics (ICARM)*, Guilin, China, Nov. 2022, pp. 854–859.

[17] Y. Chen, Y. Cai, G. Yang, H. Zhou, and J. Liu, "Neural adaptive pointing control of a moving tank gun with lumped uncertainties based on dynamic simulation," *J. Mech. Sci. Technol.*, vol. 36, no. 6, pp. 2709–2720, Jun. 2022.

[18] X. Ma, W. X. Deng, S. S. Yuan, J. Y. Yao, and G. L. Yang, "Neural network based adaptive rise control of tank gun systems," *J. Phys., Conf. Ser.*, vol. 1507, no. 5, Apr. 2020, Art. no. 052001.

[19] X. Zhou and T. Hu, "A new computed torque control system with an uncertain RBF neural network controller for a 7-DOF robot," *Tehnički Vjesnik*, vol. 27, no. 5, pp. 1492–1500, Oct. 2020.

[20] B. K. Patle, G. Babu L, A. Pandey, D. R. K. Parhi, and A. Jagadeesh, "A review: On path planning strategies for navigation of mobile robot," *Defence Technol.*, vol. 15, no. 4, pp. 582–606, Aug. 2019.

[21] S. Li, J. He, Y. Li, and M. U. Rafique, "Distributed recurrent neural networks for cooperative control of manipulators: A game-theoretic perspective," *IEEE Trans. Neural Netw. Learn. Syst.*, vol. 28, no. 2, pp. 415–426, Feb. 2017.

[22] H. Jie, G. Zheng, J. Zou, X. Xin, and L. Guo, "Adaptive decoupling control using radial basis function neural network for permanent magnet synchronous motor considering uncertain and time-varying parameters," *IEEE Access*, vol. 8, pp. 112323–112332, 2020.

[23] S. Li, M. Zhou, and X. Yu, "Design and implementation of terminal sliding mode control method for PMSM speed regulation system," *IEEE Trans. Ind. Informat.*, vol. 9, no. 4, pp. 1879–1891, Nov. 2013.

[24] A. Altan, "Performance of metaheuristic optimization algorithms based on swarm intelligence in attitude and altitude control of unmanned aerial vehicle for path following," in *Proc. 4th Int. Symp. Multidisciplinary Stud. Innov. Technol. (ISMSIT)*, Oct. 2020, pp. 1–6.

[25] A. Altan, Ö. Aslan, and R. Hacıoğlu, "Real-time control based on NARX neural network of hexarotor UAV with load transporting system for path tracking," in *Proc. 6th Int. Conf. Control Eng. Inf. Technol. (CEIT)*, İstanbul, Turkey, Oct. 2018, pp. 1–6.

[26] F.-X. Qiao, J.-P. Shi, X.-B. Qu, and Y.-X. Lyu, "Hardware-in-loop adaptive neural control for a tiltable V-tail morphing aircraft," *Defence Technol.*, vol. 22, pp. 197–211, Apr. 2023.

[27] J. Yao, Z. Jiao, D. Ma, and L. Yan, "High-accuracy tracking control of hydraulic rotary actuators with modeling uncertainties," *IEEE/ASME Trans. Mechatronics*, vol. 19, no. 2, pp. 633–641, Apr. 2014.

[28] J. Yao, Z. Jiao, B. Yao, Y. Shang, and W. Dong, "Nonlinear adaptive robust force control of hydraulic load simulator," *Chin. J. Aeronaut.*, vol. 25, no. 5, pp. 766–775, Oct. 2012.

[29] Z. Yao, J. Yao, and W. Sun, "Adaptive RISE control of hydraulic systems with multilayer neural-networks," *IEEE Trans. Ind. Electron.*, vol. 66, no. 11, pp. 8638–8647, Nov. 2019.

[30] Z. Yao, X. Liang, G.-P. Jiang, and J. Yao, "Model-based reinforcement learning control of electrohydraulic position servo systems," *IEEE/ASME Trans. Mech.*, vol. 28, no. 3, pp. 1446–1455, Jun. 2023.

[31] H. Xia, J. Chen, Z. Liu, and F. Lan, "Coordinated motion control for automated vehicles considering steering and driving force saturations," *Trans. Inst. Meas. Control*, vol. 42, no. 1, pp. 157–166, Jan. 2020.

[32] P. Zhang and Z. Wang, "Improvements of direct current motor control and motion trajectory algorithm development for automated guided vehicle," *Adv. Mech. Eng.*, vol. 11, no. 2, Feb. 2019, Art. no. 1687814018824937.

[33] J. A. Gallegos and M. A. Duarte-Mermoud, "On the Lyapunov theory for fractional order systems," *Appl. Math. Comput.*, vols. 287–288, pp. 161–170, Sep. 2016.

[34] A. Tuan Nguyen, M. Saad Rafaq, H. Ho Choi, and J.-W. Jung, "A model reference adaptive control based speed controller for a surface-mounted permanent magnet synchronous motor drive," *IEEE Trans. Ind. Electron.*, vol. 65, no. 12, pp. 9399–9409, Dec. 2018.

[35] C. J. O'Rourke, M. M. Qasim, M. R. Overlin, and J. L. Kirtley, "A geometric interpretation of reference frames and transformations: dq0, clarke, and park," *IEEE Trans. Energy Convers.*, vol. 34, no. 4, pp. 2070–2083, Dec. 2019.

[36] F. Amin, E. B. Sulaiman, W. M. Utomo, H. A. Soomro, M. Jenal, and R. Kumar, "Modelling and simulation of field oriented control based permanent magnet synchronous motor drive system," *Indonesian J. Electr. Eng. Comput. Sci.*, vol. 6, no. 2, pp. 387–395, May 2017.

[37] M. Bouazdia, M. Bouhamida, and R. Taleb, "Performance comparison of field oriented control based permanent magnet synchronous motor fed by matrix converter using PI and IP speed controllers," *Indonesian J. Electr. Eng. Comput. Sci.*, vol. 19, no. 3, pp. 1156–1168, Sep. 2020.

YIMIN WANG is currently pursuing the Ph.D. degree with the School of Mechanical Engineering, Nanjing University of Science and Technology, Nanjing, China. His current research interests include tank system dynamics, electromechanical servo control, and intelligent learning control.

SHUSEN YUAN is currently pursuing the Ph.D. degree with the School of Mechanical Engineering, Nanjing University of Science and Technology, Nanjing, China. His current research interests include complex system dynamics, servo control of mechatronic systems, and adaptive robust control.

QUANZHAO SUN received the Ph.D. degree in weapons science and technology from the Nanjing University of Science and Technology, Nanjing, China, in 2016. He was a Joint Ph.D. Student with the Department of Structural Engineering, University of California at San Diego, San Diego, CA, USA, from October 2012 to October 2013. He is currently an Associate Professor with the School of Mechanical Engineering, Nanjing University of Science and Technology. His research interests include artillery technology and armoured vehicle weapons.

XIUYE WANG received the Ph.D. degree in mechanical design and theory from the Hefei University of Technology, Hefei, China, in 2016. From September 2014 to September 2016, he visited the George W. Woodruff School of Mechanical Engineering, Georgia Institute of Technology, Atlanta, GA, USA, as a Visiting Ph.D. Student. He is currently an Associate Professor of mechanical engineering with the School of Mechanical Engineering, Nanjing University of Science and Technology. His research interests include multibody system dynamics, robust control of mechanical systems, fuzzy dynamical systems, and optimal control.

GUOLAI YANG received the Ph.D. degree in automatic weapons and ammunition engineering from the Nanjing University of Science and Technology, Nanjing, China, in 1999. He visited the Department of Mechanical Engineering, Texas Tech University, Lubbock, TX, USA, as a Visiting Professor, in 2010. He is currently a Professor of mechanical engineering with the School of Mechanical Engineering. He is also the Dean of the School of International Education, Nanjing University of Science and Technology. His research interests include theory and experimental method of time-varying mechanics, mechanical system dynamics, virtual design, and simulation technique.